Integrated Molecular Profiling of Preclinical and Clinical Cardiac Xenotransplants

Daniel Reichart

daniel.reichart@med.uni-muenchen.de

Medizinische Klinik und Poliklinik I, LMU Munich, Munich, Germany

Nastaran Hadizadeh

Department of Medicine I, LMU University Hospital, LMU Munich, Munich, Germany

Finn Becker

Department of Medicine I, LMU University Hospital, LMU Munich, Munich, Germany

Martin Bender

Department of Anaesthesiology, LMU University Hospital, LMU Munich, Munich, Germany

Jiahui Ji

Department of Medicine I, LMU University Hospital, LMU Munich, Munich, Germany

Bruno Reichart

LMU Munich

Heike Kartmann

Department of Medicine I, LMU University Hospital, LMU Munich, Munich, Germany

Vincent Albrecht

Department of Proteomics and Signal Transduction, Max Planck Institute of Biochemistry, Martinsried, Germany https://orcid.org/0009-0003-1985-7733

Jan Stöckl

Ludwig-Maximilians University of Munich https://orcid.org/0000-0002-6432-1271

Juliane Adelssen

Department of Medicine I, LMU University Hospital, LMU Munich, Munich, Germany

Asghar Ali

Center for Innovative Medical Models (CiMM), LMU Munich, Oberschleißheim, Germany
https://orcid.org/0000-0002-5137-2547

Julia Radan

University Hospital, LMU Munich

Maria Leuschen

Transregional Collaborative Research Center 127, Walter Brendel Centre of Experimental Medicine, LMU Munich, Munich, Germany

Sebastian Michel

University Hospital, LMU Munich

Elisabeth Kemter
Ludwig Maximilian University of Munich https://orcid.org/0000-0001-7785-7502
Bartley Griffith
Department of Surgery, University of Maryland Medical Center, Baltimore, MD, USA
Avneesh Singh
Department of Surgery, University of Maryland Medical Center, Baltimore, MD, USA
Barbara Kessler
Molecular Animal Breeding and Biotechnology
Mayuko Kurome
Molecular Animal Breeding and Biotechnology
Daniel DeLaughter
Department of Genetics, Harvard Medical School, Boston, MA, USA
Martin Beyer
Department of Genetics, Harvard Medical School, Boston, MA, USA
Gisella Puga Yung
University of Geneva and University Hospitals and Medical Faculty https://orcid.org/0000-0002-2283-7798
Jörg Seebach
Department of Medicine, Laboratory of Translational Immunology, Division of Immunology and Allergy, Geneva University Hospitals and Faculty of Medicine, Geneva, Switzerland
Valeria Mas
University of Maryland, Baltimore
Rabea Hinkel
German Primate Center
Joachim Denner
Institute of Virology, Free University Berlin, Berlin, Germany
Christoph Walz
Institute of Pathology, Faculty of Medicine, LMU Munich, Munich, Germany
Christian Hagl
University Hospital, LMU Munich
Steffen Massberg
University Hospital, LMU Munich https://orcid.org/0000-0001-7387-3986
Thomas Frohlich
Ludwig-Maximilians-Universität München https://orcid.org/0000-0002-4709-3211
Javier Galindo
University of Maryland School of Medicine, Baltimore, MD, USA
Andy Tully
University of Maryland School of Medicine, Baltimore, MD, USA
Alison Grazioli

University of Maryland School of Medicine, Baltimore, MD, USA
Jonathan Seidmann
Department of Genetics, Harvard Medical School, Boston, MA, USA
Christine Seidman
Harvard Medical School https://orcid.org/0000-0001-6380-1209
paolo brenner
Thierry Nordmann
Max Planck Institute of Biochemistry https://orcid.org/0000-0002-3702-815X
David Ayares
Revivicor Inc.
Jan-Michael Abicht
University Hospital, LMU Munich https://orcid.org/0000-0001-7361-1249
Matthias Mann
Max Planck Institute of Biochemistry https://orcid.org/0000-0003-1292-4799
Eckhard Wolf
Institute of Molecular Animal Breeding and Biotechnology, Gene Center, Ludwig-Maximilians-University Munich https://orcid.org/0000-0002-0430-9510
Muhammad Mohiuddin
University of Maryland School of Medicine https://orcid.org/0000-0003-4654-783X
Matthias Längin
University Hospital, LMU Munich https://orcid.org/0000-0003-0996-4941
Eric Lindberg
Department of Medicine I, LMU University Hospital, LMU Munich, Munich, Germany

---

Biological Sciences - Article

Keywords:

Posted Date: February 4th, 2026

DOI: https://doi.org/10.21203/rs.3.rs-8406985/v1

Additional Declarations: Yes there is potential Competing Interest. D.R., B.R., E.W., M.L., J.-M.A., P.B. and E.K. are co-founders of XTransplant (Starnberg, Germany). M.M.M, B.G. and A.K.S. received funding from United Therapeutics (Silver Springs, MD, USA) to perform the second transplant. M.M. is an indirect investor in Evosep Biosystems (Odense, Denmark). D.A. is founder of Revivicor Inc. (Blacksburg, VA, USA). All other authors declare no competing interests.

Abstract

Heart failure remains a leading cause of death worldwide, and the persistent shortage of donor hearts limits allogeneic cardiac transplantation. Advances in porcine genome editing, immunosuppression, and virological testing have brought cardiac xenotransplantation - the implantation of genetically engineered porcine hearts into humans - to clinical stage. The two recent first-in-human cardiac xenotransplants initially demonstrated adequate function but ended in xenograft failure [1,2], underscoring the need for mechanistic insights linked to patient outcomes.

Here, we integrate single-nucleus RNA sequencing and serial blood proteomics data to map how genetically engineered porcine hearts respond or remodel after transplantation in preclinical non-human primate models, and compare these signatures against myocardial biopsies from both human xenografts. Under optimized experimental conditions, preclinical xenografts can achieve coordinated immune and metabolic balance with preserved function. In contrast, xenografts undergoing immune rejection, virus-driven endothelial cell activation, and/or metabolic stress reveal distinct tissue injury patterns.

Across species, our preclinical model displays hallmarks of human xenografts, including near-complete immune cell replacement and conserved cardiomyocyte stress signatures, linking early clinical experience to established experimental models. Serial blood proteome profiling further distinguishes rejection from viral injury and identifies candidate biomarkers for non-biopsy, non-invasive xenograft monitoring.

This study represents the first integrated cellular and molecular comparison of preclinical and clinical cardiac xenotransplantation, revealing conserved immune, endothelial, and metabolic programs. Together, these described signatures provide a framework for understanding and predicting xenograft behavior, and guide the translation towards clinical application.

Introduction

Recent reports of successful long-term function in pig-to-human kidney xenotransplantation [3–5], together with two compassionate-use pig-to-human cardiac xenotransplants (xHTx) with sustained graft function up to 2 months before failure, highlight the promise while revealing remaining challenges of cross-species organ transplantation [1,2]. xHTx has advanced remarkably in recent years through the utilization of multi-gene edited pigs [6,7], improved organ preservation platforms [8,9], and refinement of immunosuppressive regimens [10,11], moving the field to the verge of clinical trials

In orthotopically transplanted baboon models, life-supporting pig hearts have survived beyond nine months [7]. Despite all these advances, graft dysfunction, acute rejection episodes, and porcine cytomegalovirus/roseolovirus (PCMV/PRV) [1,16–18] remain major barriers to long-lasting outcomes,

raising the question of how closely the cellular and molecular programs driving success or failure in preclinical pig-to-baboon xHTx align with those in humans [19,20].

To bridge this translational gap, we integrated single-nucleus RNA sequencing (snRNA-seq) and plasma proteomics to build a molecular atlas of pig-to-baboon and pig-to-human xHTx. Analysis of human xenograft biopsies revealed conserved immune and endothelial cell (EC) signatures closely mirroring those observed in pig-to-baboon xHTx. Upon dissecting our pig-to-baboon cohort, we showed that 3-month protocol xenografts exhibited coordinated immunological and metabolic adaptation with preserved organ function, whereas xenografts with dysfunction displayed distinct features of immune rejection, virus-driven EC and immune activation, and metabolic maladaptation. By linking myocardial remodeling with blood-based proteomics biomarkers, our integrated preclinical and clinical analyses provide a translational roadmap towards sustained and functioning xenograft function.

Determinants of cardiac xenograft outcomes in the preclinical pig-to-baboon model

Given the limited number of human xHTx cases and with the goal of extending our observations under controlled experimental conditions, we first investigate an expanded cohort of preclinical pig-to-baboon cardiac xenografts. Here, we analyze 19 orthotopic cardiac xenotransplants of genetically engineered, crossbred German Landrace and Large White pigs carrying three genetic modifications (3-GE: *GGTA1*-knockout with human *CD46* and *THBD* transgenes), transplanted into adult male baboons (*Papio anubis* and *Papio hamadryas*) maintained under established immunosuppression (Extended Data Table 1a). These genetic modifications were designed to address innate anti-Gal responses, inhibition of complement-mediated cell lysis associated with anti-non-Gal antibody responses, and xeno-induced microvascular thrombosis in the xenografts.

Based on transplantation protocol and clinical/pathological outcomes, all baboons are stratified into five cohorts (Fig. 1a): (1) ‘3-month protocol’ (n=7), with sustained graft function for 84.4±14.7 days; (2) ‘6-month protocol’ (n=3), with xenograft survival up to 195 days (mean survival: 165.7±40.1 days); (3) ‘prematurely terminated’ (n=2), with early mortality (mean survival: 0.5±0.71 days) from non-rejection complications; (4) ‘rejection’ (n=4), showing classical features of humoral or cellular rejection of the xenograft (mean survival: 67.0±70.0 days), and (5) ‘PCMV/PRV’ (n=3), recipients of hearts with detectable PCMV/PRV transcripts, associated with early xenograft dysfunction and reduced survival (mean survival: 17.7±6.8 days).

Cellular landscape and compositional changes in pig-to-baboon xHTx

We performed snRNA-seq on left ventricular (LV) free wall tissue from xenotransplanted and non-transplanted control porcine hearts [21–23]. A total of 186,947 high-quality nuclei are aligned to a hybrid pig-baboon reference genome. Unsupervised clustering identifies eleven major donor (*Sus scrofa*) and recipient-derived (*P. anubis* and *P. hamadryas*) cell types (Supplementary Fig. 1). *S. scrofa*-derived populations included cardiomyocytes (CMs), fibroblasts (FBs), mural cells (MCs), vascular endothelial cells (Vasc_ECs), endocardial/lymphatic endothelial cells (Endo/Lymph_ECs), resident immune cells

(Res_Immune), and neuronal cells (NCs). *P. anubis/hamadryas*-derived populations included infiltrating myeloids (Mye_papio), lymphoids (Lymph_papio), mast cells (Mast_papio), and baboon-specific ECs (EC_papio) [24] (Fig. 1b, Extended Data Fig. 1a-b, Supplementary Table 1-2). Across these lineages, 71 distinct cell states are resolved with unique transcriptional signatures (Extended Data Fig. 2-8, Supplementary Table 3-9); canonical cell type-specific markers are shown in Fig. 1c.

Differences in cell type abundance are assessed using centered log-ratio (CLR) transformed values, revealing a significant increase of infiltrating baboon immune cells in xenografts compared to control hearts (Fig. 1d, Extended Data Table 2). This immune influx is less pronounced in 'prematurely terminated' xenografts with short survival time, but increases over time in those with longer survival, indicating progressive infiltration with *P. anubis* and *P. hamadryas* immune cells, while the proportion of resident porcine immune cells decreases (Fig. 1e). Additionally, all macrophages (MPs) in control hearts and '3-month protocol' xenografts exhibit anti-inflammatory profiles consistent with tissue homeostasis and immunological stability, whereas 'rejection' xenografts show a shift towards pro-inflammatory dominance (Fig. 1f, Extended Data Table 3). Metabolic gene transcription profiles are also highly correlated between control hearts and '3-month protocol' xenografts (Pearson r = 0.98), both enriched for fatty acid oxidation (FAO) signatures and scoring low for metabolic dysfunction and glycolysis (Supplementary Table 10, Supplementary Data Fig. 1). At cell state level, '3-month protocol' xenografts most closely resemble the control hearts across major cell lineages, including CMs, Vasc_ECs, FBs, and resident immune cells, underscoring their suitability as a reference group with sustained xenograft function (Supplementary Fig. 2, Supplementary Table 11).

Immune dysregulation and maladaptive remodeling in rejection

The 'rejection' cohort (n=4) is characterized by profound immune dysregulation and maladaptive intercellular signaling. Infiltrating Mye_papio and Lymph_papio are expanded compared to the '3-month protocol' cohort. 'Rejection' xenografts show reduced homeostatic MP_LYVE1hi_papio and instead depict an increase in pro-inflammatory MP_ISG_papio and MP_GBE1_papio, marked by interferon-stimulated gene (ISG) induction and hypoxia-associated signatures (Fig. 2a, Extended Data Fig. 2a-c, 3a-c). A transcriptional shift toward a pro-inflammatory MP phenotype is evident across several MP states, including MP_LYVE1hi_papio and MP_TREM2_papio (Fig. 2b, Extended Data Fig. 2d, Extended Data Table 4), and pathway enrichment of infiltrating Mye_papio depicts hypoxia and apoptosis (Fig. 2c, Supplementary Table 12).

As the primary barrier to immune cell infiltration, Vasc_ECs in 'rejection' xenografts reveal markedly altered intercellular crosstalk compared with '3-month protocol' xenografts (Supplementary Table 13-15). In the latter cohort, ECs maintain vascular integrity via *JAG1-NOTCH2/3* signaling, while the 'rejection' cohort shows impaired EC signaling (Fig. 2d), alongside an elevation in vascular remodeling pathways (ANGPT, KIT, PTPRM, BMP) (Fig. 2e). In contrast to the '3-month protocol', ECs from 'rejection' xenografts are associated with remodeling pathways including VEGF, VISFATIN, HSPG and TGFβ (Extended Data Fig. 9a-b). Acting as co-receptors for TGFβ and VEGF, EC-derived HSPG signals toward

CMs, consistent with roles in xenograft vasculopathy and maladaptive remodeling. Notably, VEGF signaling is also observed between ECs and CMs, possibly downstream of HSPG induction [25,26] (Fig. 2f).

Compared to the '3-month protocol' cohort, CMs of 'rejection' xenografts depict depleted FAO and ketone metabolism scores alongside elevated lactate metabolism and metabolic dysfunction scores, reflecting metabolic stress (Extended Data Fig. 4a-d, Supplementary Table 16, Supplementary Fig. 3-4). CMs of 'rejection' xenografts exhibit notable downregulation of genes involved in Ca^{2+}-handling (*CAMK2D*, *CAMK2A*, *RYR2, CAMTA2*) and genes involved in contractile capacity (*SMTN*) (Fig. 2g). Moderate downregulation of *CAMK2D* is further confirmed by plasma protein levels. Proteomics analysis also reveals robust CHI3L1 and LGALS3 elevation, both biomarkers for heart failure and drivers of maladaptive ventricular remodeling [27,28], consistent with rejection (Supplementary Table 17-18). Moreover, the induction of UPR gene expression (*PERK*, *XBP1*, *ATF6*), endoplasmic reticulum (ER) chaperones (*HSPA5*, *HSP90B1*), ER-associated protein degradation (ERAD) components (*EDEM1*, *SEL1L*), and autophagy transcripts (*MAP1LC3B*, *SQSTM1*, *CHMP2B*) underscores ER stress in CMs in the case of rejection (Extended Data Fig. 4e-f, Extended Data Fig. 10a-b, Supplementary Table 19-20) [28–30].

PCMV/PRV-associated EC response

PCMV/PRV RNA and capsid protein expression in the myocardium are confirmed in the three cases of the 'PCMV/PRV' cohort by qRT-PCR and ELISA [19,31]. For transcriptomic analysis, the PCMV/PRV reference genome is integrated into the baboon-pig hybrid reference genome for alignment. Porcine Vasc_ECs are the predominant cell type with detectable PCMV/PRV transcripts, whereas *P. anubis*- and *P. hamadryas*-derived cells show no viral positivity (Fig. 2h). In the 'PCMV/PRV' xenografts, capillary ECs (Cap_ECs) decrease markedly, while ISG subsets (Cap_EC_ISG) expand (Fig. 2i-j). Transcriptomic profiling of Vasc_ECs also reveals enrichment of antiviral pathways, including interferon-α/γ and TNF-α-NFκB signaling (Extended Data Fig. 5a-d, Supplementary Table 21-23).

In 'PCMV/PRV' xenografts, ISG upregulation encompasses antiviral defense and immunomodulation genes (*MX1, IFIT1, ISG20*) (Fig. 2k). *MX1* and *OAS* gene family (*OAS1/2/3*) also show elevation on the protein-level, henceforth supporting an interferon-enriched immune milieu (Fig. 2l). Increased expression of pro-inflammatory cytokines and chemokines (*CXCL10, ACKR2*) in Vasc_ECs also suggests a shift towards an activated EC phenotype. Downregulation of junctional stability gene *TSPAN18*, paralleled by reduced *VWF* at transcript and protein levels, suggests impaired EC homeostasis, while significant upregulation of *SERPINE1* at transcript and protein levels is consistent with a pro-coagulant and hypofibrinolytic EC phenotype (Fig. 2k, Extended Data Fig. 5e) [16,31]. Strikingly, a distinct PCMV/PRV-positive EC subset (EC_pCMV/PRV_sus, also enriched for proliferation markers) replaces proliferative ECs (Prolif_EC), transcriptionally similar but predominantly arrested in S phase (Fig. 2m-n, Supplementary Table 24-25, Supplementary Fig. 5).

'6-month protocol' xenografts reveal hypoxia and hypertrophy

Under a revised ethical protocol, four cardiac xHTx (named ‘6-month protocol’) were prolonged beyond the standard observation time of three months (named ‘3-month protocol’). Three of them developed progressive LV hypertrophy as assessed by echocardiography, but showed no signs of rejection (Fig. 3a, Extended Data Table 1, Supplementary Table 26) [20,32]. CMs, comprising ~75% of all nuclei, shift from a canonical ventricular CM (vCM1) state towards a hypoxic state (Hypoxic_vCMs) enriched for *HIF1A*, *VEGFA*, and *PFKL* (Fig. 3b-d). Similar hypoxic reprogramming is observed in FBs, Vasc_ECs, and baboon-derived MPs, with proportional increase over time (Fig. 3e-f).

Gene set scoring further confirms a metabolic reprogramming with enrichment of glycolysis (*PFKL*, *PKM*, *ENO1*), lactate metabolism, and FAO depletion in CMs (Fig. 3g). Consistently, the abundance of PKM is also increased in the plasma proteome. In addition, CMs display increased transcript levels for hypertrophy-associated natriuretic peptides *NPPA* (1.92 $\log_2$FC) and *NPPB* (2.36 $\log_2$FC), as well as *MYBPC3* (0.92 $\log_2$FC) and *TNNT3* (1.45 $\log_2$FC). *LGALS3* is also significantly upregulated (2.72 $\log_2$FC) in CMs alongside its downstream genes *ADAMTS8* (3.66 $\log_2$FC) and *COL1A1* (3.49 $\log_2$FC), further supported by elevated LGALS3 protein levels (0.83 $\log_2$FC) in plasma (Fig. 3h, Extended Data Fig. 4d-f, Supplementary Table 27-28).

Cell-cell communication analysis further reveals exclusive activation of VISFATIN, RELN, IL-1, and HSPG (Supplementary Table 29-31). VISFATIN is predominantly received by CMs, where it may contribute to NAD^+ biosynthesis, energy metabolism, and hypoxia responses via *HIF1A*-dependent regulation [33]. Compared to ‘3-month protocol’ xenografts, NOTCH signaling is reduced in ‘6-month protocol’ xenografts. Unlike ‘3-month protocol’ xenografts, CMs from ‘6-month protocol’ xenografts reveal VEGFA signaling to ECs, and GHRELIN signals emerge from ECs and MCs. Moreover, FGF and PDGF signals from CMs toward FBs increase, while FGF signaling from FBs to CMs is reduced (Fig. 3i, Extended Data Fig. 11b-e). In line with other cell types, CMs from ‘6-month protocol’ xenografts show enrichment for hypoxia and glycolysis pathways, but also increased interferon-α/γ signaling (Fig. 3k, Supplementary Table 32-33) [34,35]. Moreover, CMs from this cohort show activation of the *IL6-gp130/JAK2-STAT1/3* axis, being consistent with reported roles of *BNIP3*-induced *IL6* signaling and downstream *NPPA/NPPB* induction, potentially leading to cardiac hypertrophy [35–38] (Extended Data Fig. 4f).

Fibroblast reprogramming in cardiac xenografts

SnRNA-seq resolves ten FB states (Fig. 4a). Myofibroblasts (Myo_vFB), nearly absent in control hearts (<0.5%), expand to ~8% in ‘3-month protocol’ xenografts and ~18% in the ‘6-month protocol’, ‘PCMV/PRV’, and ‘rejection’ cohorts. These are significantly enriched for extracellular matrix (ECM), cytoskeletal programs, and immune-interacting factors (*IL1R1*, *CCL2*, *CD44*), consistent with immune cell recruitment and scar formation (Supplementary Table 34-36). The ISG state (vFB_ISG) increases in ‘PCMV/PRV’ xenografts (~15%) and, to a lesser degree, in other xenograft cohorts (Fig. 4b). Conversely, the homeostatic_vFB1, dominant in control hearts and ‘3-month protocol’ xenografts (~53% and ~52%), is depleted by nearly half in other conditions (Extended Data Fig. 6a-c).

Transcriptionally, xenograft FBs reveal 642 DEGs relative to FBs from control hearts, posing FB transcriptional reprogramming as a central signature associated with xenograft survival or failure (Fig. 4c, Supplementary Table 37). Interestingly, FBs from the 'rejection' and 'PCMV/PRV' cohorts display the highest number of DEGs compared to FBs from '3-month protocol' xenografts (Fig. 4d). Differential expression analysis further reveals significant upregulation of genes involved in ECM remodeling (*TNC, SERPINE1*), pro-inflammatory signaling (*IL4R, CCL2*), and mechanotransduction (*YAP1*, *TEAD3/4)* (Fig. 4e). OSM-gp130 signaling scores are also elevated in FBs of xenografts, with highest levels in the 'PCMV/PRV' and 'rejection' cohorts (Fig. 4f, Supplementary Table 38) [39].

Given the central role of FBs in tissue remodeling, CellChat is applied to map fibrosis-related intercellular crosstalk. In 'rejection' xenografts, FBs reveal increased signaling toward CMs, and are enriched for remodeling pathways (*FN1, KIT, TENASCIN, PDGF*) (Fig. 4g), and receive increased growth factor inputs (*PDGF, BMP, FGF*) (Extended Data Fig. 9c-d). Proteomics further confirms a pro-fibrotic milieu with elevated porcine ECM1 (1.30 log_2FC) and COL5A3 (1.45 log_2FC). In the '6-month protocol' cohort, plasma markers of matrix turnover (*ECM1*, 1.91 log_2FC; *COL5A3*, 0.69 log_2FC; *LGALS3*, 0.83 log_2FC) are also increased (Extended Data Fig. 6d), yet FBs do not upregulate classical fibrosis programs. Instead, CMs emerge as dominant sources of remodeling and growth factor outputs (*FGF, PDGF*) (Fig. 4g). FBs, however, send elevated FGF and TENASCIN signals towards Vasc_ECs. '6-month protocol' xenografts also display enhanced VEGF, VISFATIN, HSPG, IL-1, RELN, FN1, GHRELIN, and BMP pathways compared to '3-month protocol' cohort (Extended Data Fig. 11a-e). Moreover, CMs significantly upregulate *TGFB1, COL16A1*, *COL1A1*, suggesting early-stage ECM deposition and emerging profibrotic activity (Fig. 4h, Extended Data Fig. 4f) [40]. Collectively, this data depicts a pro-fibrotic axis, including FB-driven remodeling in the 'rejection' and '6-month protocol' cohorts, as opposed to a more homeostatic profile in the '3-month protocol' cohort (Fig. 4i). Having defined the cellular and molecular programs underlying xenograft homeostasis, rejection, PCMV/PRV-associated EC activation, and hypoxia-/hypertrophy-related responses, we next investigate whether these signatures are detectable in blood and can serve as trackable markers for monitoring during the course of preclinical xHTx.

Plasma proteomics identifies early viral injury and xenograft rejection markers

To validate transcriptomic signatures and identify minimally invasive biomarkers, we performed plasma proteomics using three different protocols. Serial blood draws from baboons are obtained on average every 3-6 days during the course of preclinical xHTx. Among tested protocols, a "Beads" based enrichment yields the highest protein recovery (~1,400 proteins) and is used for downstream analysis (Extended Data Fig. 12a).

For 'PCMV/PRV', 'rejection', and '3-month protocol' conditions, Wilcoxon rank-sum testing ($p<=0.05$, $|ldFC|>=0.3$) is applied to compare blood protein abundances between the time points of transplantation and euthanasia. In 'PCMV/PRV' xenografts, 446 proteins are differentially abundant compared to the '3-month protocol' xenografts at the time of final blood draw, of which 23 are pig-derived. In the 'rejection' xenografts, 75 proteins differ significantly from those in the '3-month protocol' xenografts, including

eleven pig-derived proteins primarily originating from CMs (Extended Data Fig. 12b-c). This protein panel is then applied in a sliding-window multivariate model to determine how many days before euthanasia the outcome can be reliably predicted. An interpretable regularized linear model, trained under a leave-one-out training policy, reveals that rejection- and PCMV/PRV-associated plasma proteomics profiles can be detected 12-18 days before euthanasia, with increasing precision and F1-scores (Fig. 5a-b). For 'PCMV/PRV' xenografts, robust predictive performance is achieved across all time points after xHTx. Plasma proteomic profiles are then correlated with the time of surgery to validate their predictive potential prior to termination (Fig. 5c). Repetitive proteome-wide Spearman correlation coefficients below 0.95 indicate progressive deterioration (Supplementary Fig. 6).

Several proteins, including IFIT3, OASL, and C1QB, are specifically enriched in the baboons of the 'PCMV/PRV' cohort, and all linked to antiviral defense (Extended Data Fig. 12d). Together, these findings establish distinct rejection- and PCMV/PRV-specific plasma proteomic signatures in the preclinical setting. The signatures reflect the cellular and molecular states uncovered in our preclinical atlas and predict xenograft deterioration, providing the opportunity of timely intervention. To extend these insights and explore cross-species conservation, we next analyze myocardial biopsies from the two recent compassionate-use pig-to-human xHTx in order to directly evaluate on how preclinical models cover the clinical xenograft response.

Translation to clinical pig-to-human cardiac xHTx: insights from compassionate-use cases

In 2022 and 2023, two compassionate-use pig-to-human xHTx were performed using donor pigs carrying ten genetic modifications (10-GE). The first patient, a 57-year-old male with end-stage non-ischemic cardiomyopathy dependent on extracorporeal membrane oxygenation (ECMO) and ineligible for mechanical assist device or allogenic HTx, received a 10-GE porcine heart as previously described [2,15]. The xenograft maintained function for eight weeks but developed progressive failure on day 49, and mechanical circulatory support was withdrawn on day 60. Post-mortem analysis revealed latent PCMV/PRV in the xenograft. The second patient, a 58-year-old man with end-stage ischemic cardiomyopathy, prior coronary artery bypass grafting, and recurrent gastrointestinal bleeding, was also deemed ineligible for allogeneic HTx. After initially stable xenograft function, the patient developed progressive graft dysfunction due to rejection, requiring ECMO support by day 31. The patient chose comfort care on day 40 post-xHTx and passed away on the same day.

To elucidate the cellular and molecular mechanisms underlying these outcomes, we performed snRNA-seq on LV biopsies of both xenografts (Fig. 6a). Bioinformatic analysis yields 20,289 high-quality nuclei mapped to a hybrid human-porcine reference genome, resolving eleven major cell types (Supplementary Table 39-40). Both cases demonstrate near-complete replacement of donor porcine immune cells by recipient human immune populations (Fig. 6b-c), similar to findings in the pig-to-baboon xenografts. Compared to the first patient, the second patient depicts a pronounced expansion of human myeloid (2.72 $\log_2$FC) and lymphoid (3.11 $\log_2$FC) populations (Extended Data Fig. 13a-c, Supplementary Table

41-44). Both clinical xenografts display distinct transcriptional changes compared to non-transplanted porcine control hearts (Fig. 6d, Supplementary Table 45-48).

Comparing infiltrating human myeloid expression profiles, we identify upregulation of hypoxia-related genes (*HIF1A*, *HK2*, *PFKFB3*), ECM-remodeling factors (*SPP1*, *VCAN*, *SULF2*), innate immune mediators (*RGS1*, *CTSB*), and complement modulators (*SYK*, *C5AR1*, *DOCK4/5/8*), consistent with antibody-mediated rejection in the second patient. In addition, myeloids also show elevated MHC-II antigen presentation (*CIITA*, *CD74*). In contrast, myeloids from the first patient display strong enrichment of ISG such as *IFIT1/2/3*, *MX1/2*, *OAS1/2/3*, *IFIH1* and inflammatory cytokine genes including *CCL2* and *IL6* (Supplementary Table 48).

In the first patient, viral transcripts are confined to porcine Vasc_ECs, while all human-derived cells remain do not show PCMV/PRV positivity, confirming the lack of zoonotic transmission from the tissue to the patient. Subclustering reveals a proliferative Vasc_ECs subset (Prolif_PCMV/PRV_sus) uniquely enriched for PCMV/PRV-transcripts (Fig. 6e-f). Similar to the 'PCMV/PRV' preclinical cohort, Vasc_ECs of the first patient exhibit significant induction of cytokines (*CXCL2*, *CXCL10*, *CCL14*), ISG programs, and NFkB pathway components (*NFKBIZ*, *NFIB*). Moreover, downregulation of *VWF* and upregulation of *SERPINE1* suggest EC dysfunction and a hypofibrinolytic phenotype, consistent with observations in the preclinical model (Supplementary Table 46). Cap_ISG and Cap_NFkB Vasc_ECs subsets expand in the first patient (Extended Data Fig. 13d-f, Supplementary Table 49-50).

Beyond Vasc_EC activation, CMs of the first patient display significant enrichment of ISG programs such as *MX1* and *IFI44* (Fig. 6g), while FBs upregulated pro-fibrotic genes such as *TGFB3* (2.31 $\log_2$FC) and *TGFBR1* (1.21 $\log_2$FC) (Supplementary Table 47). Compared to the first patient, the second patient's FBs display increased expression levels of *TGFB2* (0.93 $\log_2$FC) and *TGFBR2* (1.12 $\log_2$FC) (Supplementary Table 48-50). Both patients' CMs show downregulation of contractile gene *SMTN* and Ca^{2+}-handling genes (*CAMK1A*, *ATP2A2*) (Fig. 6g).

Discussion

Two recent compassionate-use pig-to-human xHTx achieved xenograft function lasting up to two months before failing due to multifactorial causes, underscoring the feasibility and challenges of cross-species cardiac transplantation [1,2]. Building on these two cases, our integrated analysis of 19 preclinical pig-to-baboon and two clinical xenografts provides a comprehensive snRNA-seq and plasma proteomic atlas resolving the cellular and molecular programs that govern xenograft adaptation, injury, and failure.

Across preclinical and clinical settings, xHTx depict a conserved pattern of immune chimerism, which involves a near-complete replacement of donor immune populations by recipient-derived immune cells. In stable preclinical xenografts ('3-month protocol'), MPs exhibit anti-inflammatory phenotypes, consistent with effective immunosuppressive regimen maintaining effective xenograft homeostasis [41]. In contrast, MP states (MP_ISG, MP_GBE1) from 'rejection' xenografts show enhanced pro-inflammatory

signatures and are enriched for interferon, hypoxia, and apoptotic pathways, which parallel the human rejection biopsy. These data underscore that MP polarization and interferon-associated inflammation represent shared hallmarks of xenograft failure across species.

Rejection was associated with disruption of EC homeostasis, including loss of *JAG1-NOTCH2/3* signaling and enhanced activity of VISFATIN-mediated metabolic-inflammatory crosstalk, processes previously linked to xenograft vasculopathy and cytokine amplification [33,42]. In both baboon and human xenografts, PCMV/PRV-positive cases depict viral transcription primarily in porcine Vasc_ECs, accompanied by the induction of ISG, NFκB, and proinflammatory chemokines such as *IL-6, CXCL10,* and *CCL2*, indicating viral replication in this tissue [43]. Importantly, prior studies and our own data show no evidence of PCMV/PRV infection of primate or human cells [44], suggesting that the virus seems to directly and indirectly interact with immune cells and ECs to modulate cytokine expression and maladaptive remodeling in xenotransplanted recipients [18]. The high sensitivity of snRNA-seq enables the detection of these EC-restricted viral transcripts, supporting a model in which viral activation triggers interferon-mediated EC activation, impairs EC homeostasis, and promotes a pro-coagulant and hypofibrinolytic EC phenotype [16–18,31,44,45], thus contributing to xenograft failure.

CMs from 'rejection' and 'PCMV/PRV' xenografts share transcriptional signatures of contractile dysfunction, including downregulation of Ca^{2+}-handling and sarcomeric genes, together with activation of interferon-α/γ, TNFα-NF-κB, and UPR pathways [30]. In contrast, the prolonged survival '6-month protocol' xenografts exhibit progressive LV hypertrophy characterized by metabolic shift from FAO to glycolysis, and upregulation of *HIF1A*, *BNIP3*, and *IL6-gp130/JAK2-STAT1/3* signaling. The concurrent upregulation of *NPPA* and *NPPB* on transcription level, and galectin-3 (*LGALS3*) in both tissue and plasma indicate early pro-fibrotic remodeling originating from CMs [27,32,35–38]. FB reprogramming emerges as another conserved feature across species. FB activation in xenografts and expansion of vFB_ISG and Myo_FBs is associated with ECM remodeling, mechanotransduction, and *IL4/CCL2* signaling. Together, these findings highlight CM and FBs as key amplifiers of maladaptive remodeling in xenografts.

Integration of longitudinal plasma proteomics enables a functional bridge between tissue-level alterations and their systemic manifestations. Using a regularized sliding-window model, rejection-specific proteomic signatures are detectable up to 12-18 days before xenograft failure, while PCMV/PRV-associated signatures emerge shortly after xHTx. Besides using a panel of plasma proteomic markers, individual proteins discriminate viral from rejection-mediated injury, such as antiviral defense mediators IFIT3, OASL and C1QB. Taken together, these findings establish plasma proteomics as a clinically scalable tool for non-biopsy-based xenograft monitoring.

Our cross-species analyses demonstrate that the same core processes, such as immune infiltration, EC stress, viral impact, or metabolic shift, influence the xenograft homeostasis and outcomes in both baboons and humans. '3-month protocol' xenografts with stable organ function depict that immune equilibrium and metabolic adaptation are achievable, while the '6-month protocol' cohort demonstrates

the need to optimize next-generation xenografts modifications by, e.g., growth-hormone receptor knockout, utilization of smaller pig breeds, consequent viral exclusion and modulation of interferon or EC pathways.

The study is limited by its smaller sample size, cross-sectional sampling, and technical limitations of single-nucleus profiling and blood proteomics profiling. Nevertheless, by integrating cardiac single-cell and blood proteomic signatures of preclinical and clinical xHTx for the first time, this work defines conserved molecular programs of xenograft adaptation and failure. These insights improve the understanding of xenograft behavior, identify biomarkers for active xenograft surveillance, and outline a translational path towards long-lasting xenograft function in patients.

Methods

Study ethics, cohort, and animal experiments

All animal procedures complied with ethical regulations for animal research, and protocols for the preclinical model were approved by the local authorities and the Government of Upper Bavaria (approval codes: 55.2-2532.Vet_02-14-184 and ROB-55.2-2532.Vet_02-19-158). For the clinical model the United States Food and Drug Administration (FDA) approved the individual compassionate use in two cases as described before [2]. All animals were housed and handled in accordance with the Guide for the Care and Use of Laboratory Animals (US National Institutes of Health) and German legislation on the laboratory animals' welfare.

For the clinical model, donor hearts with 10-gene-edit pigs were used as described before [2]. Gene edits included knockout of the galactose-alpha1,3-galactosyltransferase (GGTA1), Sda blood group antigen (B4GALNT2), *N*-glycolylneuraminic acid (CMAH) and growth hormone receptor (GHR). Additional modifications comprised the expression of the human CD46 (hCD46), decay-accelerating factor (DAF), thrombomodulin (THBD) and endothelial cell protein C receptor (EPCR). Moreover, transgenic expression of human antiinflammatory proteins CD47 and heme oxygenase 1 (HO-1) was incorporated.

Donor hearts for the preclinical model (pig-to-baboon) were obtained from alpha1,3-galactosyltransferase GGTA1-knockout (German Landrace) juvenile pigs (German Landrace/Large White) homozygous for GGTA1-knockout, and hemizygous transgenic for human CD46 (hCD46) and human thrombomodulin (THBD) (Revivicor, Blacksburg, VA, USA and Institute of Molecular Animal Breeding and Biotechnology Gene Center, LMU Munich, Germany). Hearts were transplanted into male, captive-bred baboons (*Papio anubis (n=11)* and *hamadryas (n=9)*) obtained from the German Primate Center (DPZ, Göttingen, Germany). Expressions of hCD46/hTHBD were verified post-mortem by immunohistochemistry as previously published [12]. For organ procurement, donor pigs were sedated and anesthetized. After median sternotomy, the ascending aorta was cannulated and cross-clamped. Continuous, non-ischaemic hypothermic preservation was performed via antegrade perfusion with an oxygenated, albumin-containing hyperoncotic cardioplegic solution with erythrocytes at 8 °C and 20

mmHg, delivered via XVIVO's (XVIVO Perfusion AB, Mölndal, Sweden) extracorporeal preservation circuit (pressure/flow-controlled pump, gas exchanger, leukocyte and arterial filters, and temperature control) [9]. Recipient preparation and implantation followed the Lower Shumway technique, with intermittent graft perfusion (2 min every 15 min) during implantation.

In short, induction consisted of anti-CD20 Ab, ATG, and either anti-CD40 mAb (clone 2C10R4), anti-CD40L PAS Fab, or a combination of both antibodies as described elsewhere in detail (see Extended Data Table 1 for regimens). Maintenance immunosuppression consisted of mycophenolate mofetil, either anti-CD40 mAb (clone 2C10R4), anti-CD40L PAS Fab, or a combination of both antibodies, and methylprednisolone. All animals received anti-inflammatory therapy with an IL-6-receptor antagonist, THF inhibitor and IL-1-receptor antagonist, and an additive therapy with temsirolimus (Pfizer, New York, NY, USA) and an antihypertensive medication (enalapril (Hexal AG, Holzkirchen, Germany) and metoprolol (AstraZeneca, Cambridge, UK)) to inhibit graft overgrowth.

Xenograft function and growth were monitored with transthoracic echocardiographic examinations at regular intervals. End diastolic (EDV) and end systolic volumes (ESV), LV end diastolic (LVEDD) and end systolic diameters (LVESD), and interventricular septum thickness (IVSd) and posterior wall thickness at end diastole (PWd) were measured. LV mass, LV mass increase, and ejection fraction (EF) were calculated using formulas (1), (2), and (3), respectively.

(1) $\text{LV mass (g)} = 0.8\ (1.04\ ((\text{LVEDD} + \text{IVSd} + \text{PWd})^3 - \text{LVEDD}^3)) + 0.6$

(2) $\text{LV mass increase} = (\text{LV mass}_{\text{end}}/\text{LV mass}_{\text{start}}) - 1$

(3) $\text{EF (\%)} = 100\ ((\text{EDV} - \text{ESV}) / \text{EDV})$

Tissue acquisition and single-nuclei isolation

Cardiac xenografts were explanted post-mortem, and full-thickness samples from the left-ventricular free wall were snap-frozen in liquid nitrogen and stored at −80 °C. All processing steps were performed on ice or at 4 °C to preserve RNA integrity.

Single nuclei were isolated from flash-frozen LV free walls by mechanical homogenization. Approximately 1-4 mg tissue fragments were processed as previously described (HCA, DCM study). The pellet was resuspended in storage buffer (PBS, 4% BSA, 0.2 U μl^{-1} RNase inhibitor (Promega, Madison, WI, USA)), stained with Hoechst using NucBlue (Thermo Fisher, Waltham, MA, USA), and Hoechst+ nuclei using FACSAria Fusion (BD Biosciences, Franklin Lakes, NJ, USA) at 4°C. Nuclear integrity and yield were confirmed microscopically.

Single-nucleus 3' gene expression libraries were generated using Chromium Single Cell 3' Reagent Kits v3.1 (10X Genomics, Pleasanton, CA, USA) according to the manufacturer's protocol. Sorted nuclei were loaded onto the Chromium Controller for droplet encapsulation and reverse transcription. cDNA and libraries were quality-checked using a Bioanalyzer High Sensitivity DNA Analysis kit (Agilent

Technologies, Santa Clara, CA, USA), and quantified using the KAPA Library Quantification Kit (Roche, Basel, Switzerland). Sequencing was performed on a HighSeq/NovaSeq at Helmholtz and a Nextseq 2000 (Illumina, San Diego, CA, USA) at LAFUGA (Gene Center Munich, LMU), targeting 20,000 reads per nucleus.

Blood collection and plasma proteome enrichment

Baboon blood draws were collected at day seven and day two before the xenotransplantation, shortly before the xenotransplantation, and every 3-6 days post-transplantation into 10ml EDTA/citrate-treated tubes (Sarstedt, Nümbrecht, Germany). After collection, the tubes were inverted to ensure thorough mixing of the anticoagulant and then centrifuged at 1,000-2,000g for 10 min at 4°C. The plasma supernatant was transferred and aliquoted into new polypropylene tubes and stored at -80°C.

The plasma preparation workflows described below were automated using an Agilent Bravo Liquid Handling Platform as previously described [46]. The lysis buffer mentioned below contained 40mM chloroacetamide, 20 mM DTT, 0.01% DDM, and 60 mM TEAB. All three sample preparation workflows were applied as previously described [46,47]. Neat Plasma workflow: 1µl of baboon plasma was combined with 50 µl lysis buffer (100 mM Tris pH 8.0; 40 mM chloroacetamide; 10 mM TCEP). Samples were transferred into a Thermomixer C and heated at 95°C for 10min with agitation. After cooling to room temperature, a 10 µl digestion buffer (8µl Lysis buffer; 0.5µg Trypsin; 0.5µg Lys-C) was added and proteins underwent tryptic digestion at 37°C for 16 hours. Tryptic digest was terminated with a final concentration of 0.2% TFA.

Perchloric acid precipitation workflow with neutralization (PCA-N): 25µl of ddH20 were added to 5µl of baboon plasma, followed by the addition of 25µl 1M perchloric acid. After 1h incubation at 4°C, samples were centrifuged at 4,000g for 20min. The pH of the obtained supernatant was then adjusted to 8-8.5 by adding 8µl 1.4M sodium hydroxide solution, followed by the addition of 8µl of lysis buffer. Proteins were subsequently reduced, alkylated and denatured at 95°C for 10min using DTT (10mM final concentration) and CAA (40mM final concentration) in a TEAB buffer (pH 8-8.5, 60mM). DDM (0.01%) was used as a detergent ensuring compatibility with subsequent C18-based peptide desalting. Proteins were digested using 0.8µg Trypsin and 0.125µg LysC. Tryptic digestion was stopped with TFA (final concentration 0.5%).

The bead workflow utilized non-magnetic beads (OmniProt™, Westlake Omics), requiring centrifugation at 4000 × g for 20 min for all washing and collection steps. Beads were resuspended and washed in PBS. Plasma protein binding was performed in PBS containing 0.05% CHAPS, followed by washing of bead-bound proteins with 33% PBS. Proteins were denatured, reduced, and alkylated while bound to the beads by adding lysis buffer (33.3 µL; 40 mM chloroacetamide, 20 mM DTT, 0.01% DDM, 60 mM TEAB). Digestion proceeded as described for the neat workflow, resulting in peptide elution from the beads. The eluted peptides were acidified and analyzed by LC-MS/MS.

Data acquisition by mass spectrometry

All samples were analyzed within one batch to avoid batch effects. Within this batch, quality control samples were analyzed regularly throughout the process to monitor system stability. The Evosep One liquid chromatography system, coupled to an Orbitrap Astral mass spectrometer, was used to analyze baboon plasma samples as previously described [48]**.** Samples were chromatographically separated using the '100 samples per day' method employing an 11.5 min chromatographic gradient on an 8cm Aurora Rapid XT UHPLC column (AUR3-80150C18-XT, Ionopticks) at 50°C. Mobile phases consisted of 0.1% formic acid in water (buffer A) and 0.1% formic acid in acetonitrile (buffer B). 200ng peptides per sample were loaded onto C-18 tips (Evotip Pure, Evosep), followed by a data-independent acquisition (DIA) method [49]. The ionization source operated in positive ion mode with a fixed spray voltage of 1900V, with an ion transfer tube temperature of 280°C. High-field asymmetric waveform ion mobility spectrometry (FAIMS) was employed at "standard resolution mode" (compensation voltage of -40 V, carrier gas flow 3.5 L/min). For analyte detection, MS1 spectra were collected in the Orbitrap analyzer (resolving power 120,000 FWHM, scan range 380-980 m/z). RF lens was set to 40%. Automatic gain control (AGC) was normalized to 500% (injection time 3ms).

DIA was performed over the same scan range, using 150 isolation windows with 4 Th each, including window placement optimization. Higher energy collisional dissociation (HCD) was implemented for MS2 scans with a collision energy of 25%, an AGC target 500% and 7ms maximum injection time. Fragment ion scan range was set to 150-2000 m/z. MS1 data were acquired in profile mode, while MS2 data were recorded in centroid mode. The expected chromatographic peak width was set to 5s, and advanced peak determination was enabled for duty cycle optimization.

Single-nuclei data processing and mapping

Raw sequencing data were demultiplexed and converted to FASTQ files using *bcl2fastq* (v2.20, Illumina). Alignment and gene quantification were performed with Cell Ranger provided by 10x Genomics (v7.1.0). Reads were mapped against a custom combined reference comprising porcine (*Sus scrofa*, Ensembl release Sscrofa11.1), baboon (*Papio anubis*, Ensembl release Ens110), and PCMV/PRV, NCBI accession number: GCF_000913455.1) genomes. Before combining, the Sscrofa11.1 gtf file was modified by adding the annotations for 51 porcine genes with human homologs that have known transcription in adult hearts (Supplementary Table 51). Pre-mRNA references were generated following 10X Genomics guidelines, incorporating both exonic and intronic reads. Reads with ambiguous alignments to multiple genomic features were excluded from quantification by the Cellranger pipeline.

Data processing and quality control

For both preclinical and clinical samples, Cellbender was applied to remove ambient RNA and potential signals of false-positive cross-species hybrid cells using the remove-background function (v0.3.0). Cellbender-called nuclei-containing droplets were used for downstream analysis. Quality control and downstream analyses were conducted in Scanpy (v.1.11.1) [50]. Doublets were identified and removed using Solo (v.0.3). Additionally, Scrublet scores were calculated with prior z- and log-transformation as

an independent method (v.0.2.1) [51,52]. In clinical xHTx, nuclei with total UMI counts (total_counts) < 40,000, number of detected genes (n_genes_by_counts) between 200 and 5,000, mitochondrial transcript fraction<1%, ribosomal genes <1%, and softmax Solo scores<0.5 were retained for further analysis (Supplementary Fig. 7-8). In preclinical samples, nuclei with 4,000<total_counts<10,000, 200<n_genes<5,000, mitochondrial transcript fraction <1%, ribosomal genes <1%, and softmax Solo scores<0.5 were kept for downstream analysis (Supplementary Fig. 9-10).

Highly variable genes were identified on normalized log-transformed counts. Data were scaled to unit variance, principal component analysis was computed, and a neighborhood was constructed. Batch effects were corrected with “Sample_ID” as batch_key using Harmony (v.1.11.3) [53]. UMAP was used for visualization, and the Leiden algorithm for nuclei clustering [54]. To identify cell type-specific expression differences, differential gene expression analysis was performed using the two-sided Wilcoxon rank-sum test and Bonferroni-Hochberg (BH) adjustment as implemented in the Scanpy framework. Significant DEGs of each cluster were identified by *FDR*< 0.05, |log2FC|>0.5 and used for manual cell type annotation, followed by subclustering to identify cell states.

Differential gene expression of pseudobulked snRNAseq gene expression data

For condition-specific comparisons of the preclinical samples, pseudobulks were generated per cell type and state. Differential gene expression analysis on pseudobulk expression values was performed using edgeR (v3.28.1) [21,23,55]. Genes with mean expression (log transformed and library size normalized) of higher than 0.0125 (in each condition) were tested for differential expression. Rare cell states (<5 nuclei in at least three samples) were excluded. Differentially expressed genes were marked by FDR<5% and |log2FC|>0.5.

For the human xHTx analysis, cell type-specific differentially expressed genes (DEGs) were identified by performing pairwise comparisons across the conditions (e.g., xHTx1 vs. control, xHTx2 vs. control, and xHTx1 vs. xHTx2) using FindMarkers function in Seurat (version 5.3.0). The analysis was conducted on the SCT assay data (the 'data' slot) using the default Wilcoxon rank-sum test. Only genes expressed in a minimum of 0.1% of cells in either of the two comparison groups were tested. We applied an initial filtering threshold of |log2FC| threshold of 0.1 with least log-scaled 0.1-fold difference between groups. The resulting P-values were adjusted for multiple testing using the Benjamini-Hochberg method to calculate FDR. Genes with FDR<5% and |log2FC|>0.5 were considered statistically significant DEGs.

Differential plasma protein abundance analysis and modelling

The raw output files were processed using DIA-NN (v2.0). The searches were performed against the reference proteomes from UniProt for baboon (UP000028761) and pig (UP000008227) fasta files (retrieval data 16.05.2025). Additionally, fasta files comprising virus sequences were added: Suid betaherpesvirus 2 (UP000243849), BaCMV (UP001151210), Porcine Circovirus (UP000000470), Baboon Herpesvirus / CeHV-12 (UP000326414), Herpesvirus Papio 2 / CeHV-16 (UP000130066), Human Hepatitis E (UP000007243), Human Epstein-barr virus (UP000153037), PERV-A (UP000101055), PERV-B

(UP000104185), porcine lymphotropic herpesvirus (in silico translated using genome assembly and annotation https://ncbi.nlm.nih.gov/datasets/genome/GCF_002814915.1/). Proteotypicity was set to Genes (species-specific), scan window to 5, MS1 accuracy to 4 ppm and MS2 accuracy to 10 ppm. The 100 largest files were searched first and using the match between runs (MBR) feature a spectral library was generated. Afterwards all runs were searched against this library without MBR. Data analysis was then performed using the main report.

Proteomic quantification data were log-transformed and analyzed to assess protein abundance differences across experimental conditions. For each protein, preprocessed intensities were compared between each condition and the Standard-protocol group. Statistical comparisons were conducted using the two-sided Mann–Whitney U test and multiple testing correction was applied across all pairwise comparisons using the Benjamini-Hochberg method. In each comparison, proteins with FDR<5% and |log2FC|>0.5 were considered statistically significant. For time-course modelling, L1-regularized logistic regression in a sliding-window approach was applied on imputed intensities (KNNImputer, implemented in sklearn.impute), with timepoint of euthanasia being the common anchor timepoint. Accuracy, precision and F1-scores were computed using a LOO-CV (leave-one-out cross-validation) policy in each sliding-window. For the correlation analysis, pairwise spearman correlation coefficients were computed between all samples and the blood sample taken at the day of surgery (Day 0) from the same baboon.

Differential abundance analysis of snRNA-seq identified cell-types and -states

Cell type/state abundance differences were analyzed using the centered log-ratio (CLR) transformation of proportional cell counts, as previously described [21]. In short, absent cell-types per sample were imputed using the geometric Bayesian multiplicative replacement method via zCompositions package (v.1.5.0.4) [56]. Linear models were fitted to CLR-transformed values where the condition was used as an indicator variable, using either the control or the 3-month protocol group as the reference.

Significance was assessed using a two-sided t-test (corrected for Benjamini-Hochberg). Pairwise comparisons of cell type and state abundances between conditions were performed using the Wilcoxon rank-sum test with BH FDR correction. Only samples with ≥10 cells per tested category were included.

Pathway and gene enrichment analysis

Pathway enrichment was performed using the gseapy package (v.1.1.8) [57] with the Molecular Signatures Database ‘MSigDB_Hallmark_2020’ gene set collection with the default background gene set. For each comparison, up- and down-regulated DEGs were analyzed separately. Enrichment was run with Enrichr defaults, and pathways with an adjusted P value (FDR) <0.05 were considered significant [58].

Gene set score enrichment

Gene set enrichment scores were computed using the score_genes function in Scanpy on log-normalized and scaled expression matrices [50]. Four curated gene sets derived from published literature were evaluated: metabolic pathways [59], macrophage pro/anti-inflammatory signatures [60], and the OSM pathway [39]. Cell cycle phase scoring (S and G2/M) was performed using the pre-defined canonical gene lists [61] implemented in Scanpy.

Cell-cell communication analysis

Intercellular networks were inferred using CellChat (v1.6.1) [62]. For each condition, Seurat objects were converted to CellChat objects (createCellChat) using the CellChatDB.human ligand-receptor database. Overexpressed genes and ligand–receptor pairs were identified with identifyOverExpressedGenes() and identifyOverExpressedInteractions(). Communication probabilities were estimated with computeCommunProb() using type ="triMean", which provides a robust group-level expression estimate and reduces the influence of outliers. The resulting networks were filtered with filterCommunication(), retaining only interactions in which both ligand and receptor were expressed in at least five nuclei within the relevant cell types (min.cells=5). Pathway-level probabilities were computed with computeCommunProbPathway(), and networks were aggregated using aggregateNet() to quantify total information flow per signaling pathway. Centrality analyses were performed with netAnalysis_computeCentrality (slot.name="netP") to identify dominant sender, receiver, mediator, and influencer cell types within the inferred communication networks.

For differential cell-cell communication analysis, CellChat objects were harmonized using liftCellChat() and merged with mergeCellChat(). Differential pathway activity and signaling strength were quantified using rankNet() in comparison mode with statistical testing ($p \leq 0.05$). Communication tables for each condition were exported, and differential signaling contributions were summarized across cell types. Standard CellChat visualization functions were complemented with Circos plots generated using the circlize package [63].

Statistics and reproducibility

Analyses were performed in Python (v3.10.12) and R (v4.3.3). Details for statistical testing are provided in the figure legends. Sample sizes were not pre-calculated prior to experiments, and no samples were excluded. All snRNA-seq analyses, including clustering, were done using unbiased techniques. The experiments were not randomized, and investigators were not blinded to allocation during experiments and outcome assessment.

Declarations

Acknowledgment

We gratefully acknowledge the LAFUGA at the Gene Center, LMU Munich, the Core Facility Flow Cytometry at the Biomedical Center, LMU Munich, and the Helmholtz Sequencing Facility for providing

equipment, services, and expertise. We also thank LMU University Hospital for providing computing resources on their Clinical Open Research Engine (CORE). Revivicor kindly provided 10-GE donor pigs for the human xHTx. Eledon (Irvine, CA, USA) and Kiniksa Pharmaceuticals (Lexington, MA, USA) supplied anti-CD40L and anti-CD40 antibodies, respectively, for the human xHTx. XVIVOPerfusion AB (Mölndal, Sweden) kindly provided cardiac preservation support.

Author contributions

These authors contributed equally: Nastaran Hadizadeh, Finn Becker and Martin Bender.

These authors jointly supervised this work: Daniel Reichart, Eric L Lindberg, Matthias Längin and Muhammad M Mohiuddin.

Conceptualization: B.R., E.W., M.M.M., M.L., E.L.L. and D.R.; Methodology: N.H., F.B., M.Be, J.J., B.R., H.K., V.A., J.B.S., J.A., A.A., J.R., M.L., S.M., E.K., B.P.G., A.K.S, B.K., M.K., D.D., M.Ba., G.P.Y., J.D.S., J.D., C.W., T.F., J.G., A.T., A.G., P.B., J.G.S, C.E.S., T.M.N., D.A., V.R.M., J.-M.A., M.M., E.K., E.W., M.M.M., M.L., E.L.L. and D.R.; Formal analysis: N.H., F.B., M.Be., J.J., V.A., J.B.S., D.D., M.Ba., G.P.Y., J.D., C.W., T.M.N., J.-M.A., M.L., E.L.L. and D.R.; Investigation: N.H., F.B., M.Be., J.J., B.R., H.K., V.A., J.B.S., J.A., A.A., B.P.G., A.K.S, G.P.Y., J.D.S., J.D., C.W., T.F., J.G., A.T., A.G., J.G.S, C.E.S., T.M.N., D.A., V.R.M., J.-M.A., M.M., E.W., M.M.M., M.L., E.L.L. and D.R.; Resources: M.Be., B.R., H.K., J.B.S., A.A., J.R., M.L., S.M., E.K., B.P.G., A.K.S, B.K., M.K., V.R.M., R.H., C.W., C.H., S.M., T.F., J.G., A.T., P.B., T.M.N, D.A., J.-M.A., E.W., M.M.M., M.L. and D.R.; Writing original draft: N.H., F.B., M.Be., J.J., E.W., M.L., E.L.L. and D.R.; Reviewing original draft: M.Be., B.R., H.K., V.A., J.B.S., J.A., A.A., J.D., S.M., T.F., T.M.N., D.A., J.-M.A., M.M. and M.M.M.; Visualization: N.H., F.B., J.J., G.P.Y., M.L., E.L.L., and D.R.; Supervision: B.R., T.M.N., J.-M.A., M.M., E.W., M.M.M., M.L., E.L.L. and D.R.; Funding acquisition: B.R., P.B., D.A., J.-M.A., M.M., E.W., M.M.M., M.L. and D.R.

Conflicts of interest

D.R., B.R., E.W., M.L., J.-M.A., P.B. and E.K. are co-founders of XTransplant (Starnberg, Germany). M.M.M, B.G. and A.K.S. received funding from United Therapeutics (Silver Springs, MD, USA) to perform the second human transplant. M.M. is an indirect investor in Evosep Biosystems (Odense, Denmark). D.A. is founder of Revivicor Inc. (Blacksburg, VA, USA). All other authors declare no competing interests.

Data availability

All data generated and analyzed in this study will be deposited at the European Nucleotide Archive (ENA) (https://www.ebi.ac.uk/ena/browser/home), which is hosted by the European Bioinformatics Institute (EMBL-EBI). Raw data can be downloaded from the ENA upon publication under project PRJEB105676. Processed single-nucleus transcriptomic and proteomic data will be available through Zenodo in the h5ad and csv format upon publication and will be provided upon request. Metadata sheets are available in Extended Data Table 1.

Code availability

All code used to generate the figures in this publication are available on GitHub (https://github.com/nastaran-hadizadeh/Xenotransplant). All scripts run on Jupyter notebooks are available as .ipynb files, and scripts executed in the command line are available as .txts, .sh, or .py files. R scripts are available as .R. The singularity container with the software environment was deposited on github in the .sif format.

References

1. Moazami, N. *et al.* Pig-to-human heart xenotransplantation in two recently deceased human recipients. *Nat. Med.* **29**, 1989–1997 (2023).
2. Griffith, B. P. *et al.* Genetically Modified Porcine-to-Human Cardiac Xenotransplantation. *N. Engl. J. Med.* **387**, 35–44 (2022).
3. Montgomery, R. A. *et al.* Physiology and immunology of pig-to-human decedent kidney xenotransplant. *Nature* 1–3 (2025).
4. Lee, S. A. *et al.* Physiologic Homeostasis in a Living Human after Pig Kidney Xenotransplantation. *Nat. Commun.* **16**, 1–10 (2025).
5. Schmauch, E. *et al.* Multi-omics analysis of a pig-to-human decedent kidney xenotransplant. *Nature* 1–3 (2025).
6. Hinrichs, A. *et al.* Growth hormone receptor knockout to reduce the size of donor pigs for preclinical xenotransplantation studies. *Xenotransplantation* **28**, (2021).
7. Mohiuddin, M. M. *et al.* Progressive genetic modifications of porcine cardiac xenografts extend survival to 9 months. *Xenotransplantation* **29**, (2022).
8. Längin, M. *et al.* Cold non-ischemic heart preservation with continuous perfusion prevents early graft failure in orthotopic pig-to-baboon xenotransplantation. *Xenotransplantation* **28**, (2021).
9. Rega, F. *et al.* Hypothermic oxygenated perfusion of the donor heart in heart transplantation: the short-term outcome from a randomised, controlled, open-label, multicentre clinical trial. *Lancet* **404**, 670–682 (2024).
10. Mohiuddin, M. M. *et al.* Chimeric 2C10R4 anti-CD40 antibody therapy is critical for long-term survival of GTKO.hCD46.hTBM pig-to-primate cardiac xenograft. *Nat. Commun.* **7**, (2016).
11. Phillips, K. G. *et al.* Cardiac Xenotransplantation: Current State and Future Directions. *Circulation* **152**, 58–73 (2025).
12. Reichart, B. *et al.* Cardiac xenotransplantation: from concept to clinic. *Cardiovasc. Res.* **118**, 3499–3516 (2022).
13. Cleveland, J. D., Mitchell, C., Cooper, D. K. C. & Cleveland, D. C. The potential of cardiac xenotransplantation for management of infants with complex congenital heart disease. *Transl. Pediatr.* **12**, 2247–2255 (2023).
14. Mitchell, C. B. *et al.* Early Results of an Infant Model of Orthotopic Cardiac Xenotransplantation. *J. Heart Lung Transplant.* **44**, 503–510 (2025).

15. Mohiuddin, M. M. *et al.* Graft dysfunction in compassionate use of genetically engineered pig-to-human cardiac xenotransplantation: a case report. *Lancet* **402**, 397–410 (2023).
16. Denner, J. *et al.* Impact of porcine cytomegalovirus on long-term orthotopic cardiac xenotransplant survival. *Sci. Rep.* **10**, (2020).
17. Denner, J. OMICS Analyses in Xenotransplantation: Initial Findings, Key Precautions, and Virus Infections. *Xenotransplantation* **32**, (2025).
18. Denner, J. How Does a Porcine Herpesvirus, PCMV/PRV, Induce a Xenozoonosis. *Int. J. Mol. Sci.* **26**, (2025).
19. Reichart, B. *et al.* Pig-to-non-human primate heart transplantation: The final step toward clinical xenotransplantation? *J. Heart Lung Transplant.* **39**, 751–757 (2020).
20. Bender, M. *et al.* Hemodynamics in pig-to-baboon heterotopic thoracic cardiac xenotransplantation: Recovery from perioperative cardiac xenograft dysfunction and impairment by cardiac overgrowth. *Xenotransplantation* **31**, (2024).
21. Reichart, D. *et al.* Pathogenic variants damage cell composition and single cell transcription in cardiomyopathies. *Science* **377**, (2022).
22. Litviňuková, M. *et al.* Cells of the adult human heart. *Nature* **588**, 466–472 (2020).
23. Maatz, H. *et al.* The cellular and molecular cardiac tissue responses in human inflammatory cardiomyopathies after SARS-CoV-2 infection and COVID-19 vaccination. *Nat. Cardiovasc. Res.* **4**, 330–345 (2025).
24. Miao, J. *et al.* Single-nucleus transcriptomics reveal cardiac cell type-specific diversification in metabolic disease transgenic pigs. *iScience* **27**, 110015–110015 (2024).
25. Daly, K. P. *et al.* Vascular endothelial growth factor A is associated with the subsequent development of moderate or severe cardiac allograft vasculopathy in pediatric heart transplant recipients. *J. Heart Lung Transplant.* **36**, 434–442 (2017).
26. Pretorius, D., Richter, R. P., Anand, T., Cardenas, J. C. & Richter, J. R. Alterations in heparan sulfate proteoglycan synthesis and sulfation and the impact on vascular endothelial function. *Matrix Biol. Plus* **16**, 100121 (2022).
27. Kim, S. H. *et al.* Chlorogenic acid attenuates cardiac hypertrophy and fibrosis by downregulating galectin 3. *Sci. Rep.* **15**, 1–16 (2025).
28. Stephan, J. K. *et al.* Neutrophil-secreted CHI3L1 exacerbates cardiac dysfunction and inflammation after myocardial infarction. *FASEB J.* **39**, (2025).
29. Wang, X., Xu, L., Gillette, T. G., Jiang, X. & Wang, Z. V. The unfolded protein response in ischemic heart disease. *J. Mol. Cell. Cardiol.* **117**, 19–19 (2018).
30. Liu, M. *et al.* Activation of the unfolded protein response downregulates cardiac ion channels in human induced pluripotent stem cell-derived cardiomyocytes. *J. Mol. Cell. Cardiol.* **117**, 62–71 (2018).

31. Bender, M. *et al.* The Endothelial Glycocalyx in Pig-to-Baboon Cardiac Xenotransplantation—First Insights. *Biomedicines* **12**, 1336–1336 (2024).
32. Längin, M. *et al.* Xenografts Show Signs of Concentric Hypertrophy and Dynamic Left Ventricular Outflow Tract Obstruction after Orthotopic Pig-to-baboon Heart Transplantation. *Transplantation* **107**, E328–E338 (2023).
33. Hu, Y. *et al.* Visfatin Amplifies Cardiac Inflammation and Aggravates Cardiac Injury via the NF-κB p65 Signaling Pathway in LPS-Treated Mice. *Mediators Inflamm.* **2022**, 3306559–3306559 (2022).
34. Sant'Ana, P. G. *et al.* Hypoxia-Inducible Factor 1-Alpha and Glucose Metabolism during Cardiac Remodeling Progression from Hypertrophy to Heart Failure. *Int. J. Mol. Sci.* **24**, (2023).
35. Raj Murthi, S. *et al.* Contribution of hypoxia-inducible factor 1alpha to pathogenesis of sarcomeric hypertrophic cardiomyopathy. *Sci. Rep.* **15**, 1–22 (2025).
36. Chaanine, A. H. *et al.* Potential role of BNIP3 in cardiac remodeling, myocardial stiffness, and endoplasmic reticulum mitochondrial calcium homeostasis in diastolic and systolic heart failure. *Circ. Heart Fail.* **6**, 572–583 (2013).
37. Weng, Y. J. *et al.* BNIP3 induces IL6 and calcineurin/NFAT3 hypertrophic-related pathways in H9c2 cardiomyoblast cells. *Mol. Cell. Biochem.* **345**, 241–247 (2010).
38. Crow, M. T. Hypoxia, BNip3 proteins, and the mitochondrial death pathway in cardiomyocytes. *Circ. Res.* **91**, 183–185 (2002).
39. Dey, G. *et al.* Signaling network of Oncostatin M pathway. *J. Cell Commun. Signal.* **7**, 103–103 (2012).
40. Heras-Bautista, C. O. *et al.* Cardiomyocytes facing fibrotic conditions re-express extracellular matrix transcripts. *Acta Biomater.* **89**, 180–192 (2019).
41. Kopecky, B. J. *et al.* Donor Macrophages Modulate Rejection after Heart Transplantation. *Circulation* **146**, 623–623 (2022).
42. Li, Y., Hiroi, Y. & Liao, J. K. Notch Signaling as an Important Mediator of Cardiac Repair and Regeneration after Myocardial Infarction. *Trends Cardiovasc. Med.* **20**, 228–228 (2010).
43. Zhang, G. *et al.* The role of interleukin-6 (IL-6) in the systemic inflammatory response in xenograft recipients and in pig kidney xenograft failure. *Front. Immunol.* **12**, 788949 (2021).
44. Denner, J. Reduction of the survival time of pig xenotransplants by porcine cytomegalovirus. *Virology Journal 2018 15:1* **15**, 1–7 (2018).
45. Gollackner, B. *et al.* Porcine cytomegalovirus and coagulopathy in pig-to-primate xenotransplantation. *Transplantation* **75**, 1841–1847 (2003).
46. Albrecht, V., Müller-Reif, J. B., Brennsteiner, V. & Mann, M. A simplified perchloric acid workflow with neutralization (PCA N) for democratizing deep plasma proteomics at population scale. *Mol. Cell. Proteomics* 101071–101071 (2025).
47. Korff, K. et al. Pre-analytical drivers of bias in bead-enriched plasma proteomics. bioRxiv (2025) doi:10.1101/2025.05.07.652495.

48. Wahle, M. *et al.* A Novel Hybrid High-Speed Mass Spectrometer Allows Rapid Translation From Biomarker Candidates to Targeted Clinical Tests Using 15N-Labeled Proteins. *Mol. Cell. Proteomics* **24**, 101050–101050 (2025).
49. Guzman, U. H. *et al.* Ultra-fast label-free quantification and comprehensive proteome coverage with narrow-window data-independent acquisition. *Nat. Biotechnol.* **42**, 1855–1866 (2024).
50. Wolf, F. A., Angerer, P. & Theis, F. J. SCANPY: Large-scale single-cell gene expression data analysis. *Genome Biol.* **19**, 1–5 (2018).
51. Bernstein, N. J. *et al.* Solo: Doublet Identification in Single-Cell RNA-Seq via Semi-Supervised Deep Learning. *Cell Syst.* **11**, 95–101.e5 (2020).
52. Wolock, S. L., Lopez, R. & Klein, A. M. Scrublet: Computational Identification of Cell Doublets in Single-Cell Transcriptomic Data. *Cell Syst.* **8**, 281–291.e9 (2019).
53. Korsunsky, I. *et al.* Fast, sensitive and accurate integration of single-cell data with Harmony. *Nat. Methods* **16**, 1289–1296 (2019).
54. Traag, V. A., Waltman, L. & van Eck, N. J. From Louvain to Leiden: guaranteeing well-connected communities. *Sci. Rep.* **9**, 1–12 (2019).
55. Robinson, M. D., McCarthy, D. J. & Smyth, G. K. edgeR: a Bioconductor package for differential expression analysis of digital gene expression data. *Bioinformatics* **26**, 139–140 (2010).
56. Martín-Fernández, J. A., Hron, K., Templ, M., Filzmoser, P. & Palarea-Albaladejo, J. Bayesian-multiplicative treatment of count zeros in compositional data sets. *Stat. Modelling* **15**, 134–158 (2015).
57. Subramanian, A. *et al.* Gene set enrichment analysis: a knowledge-based approach for interpreting genome-wide expression profiles. *Proc. Natl. Acad. Sci. U. S. A.* **102**, 15545–15550 (2005).
58. Fang, Z., Liu, X. & Peltz, G. GSEApy: a comprehensive package for performing gene set enrichment analysis in Python. *Bioinformatics* **39**, (2023).
59. Liberzon, A. *et al.* The Molecular Signatures Database Hallmark Gene Set Collection. *Cell Syst.* **1**, 417–425 (2015).
60. Xue, J. *et al.* Transcriptome-Based Network Analysis Reveals a Spectrum Model of Human Macrophage Activation. *Immunity* **40**, 274–288 (2014).
61. Tirosh, I. *et al.* Dissecting the multicellular ecosystem of metastatic melanoma by single-cell RNA-seq. *Science* **352**, 189–196 (2016).
62. Jin, S. *et al.* Inference and analysis of cell-cell communication using CellChat. *Nat. Commun.* **12**, 1–20 (2021).
63. Gu, Z., Gu, L., Eils, R., Schlesner, M. & Brors, B. circlize Implements and enhances circular visualization in R. *Bioinformatics* **30**, 2811–2812 (2014).

Figures

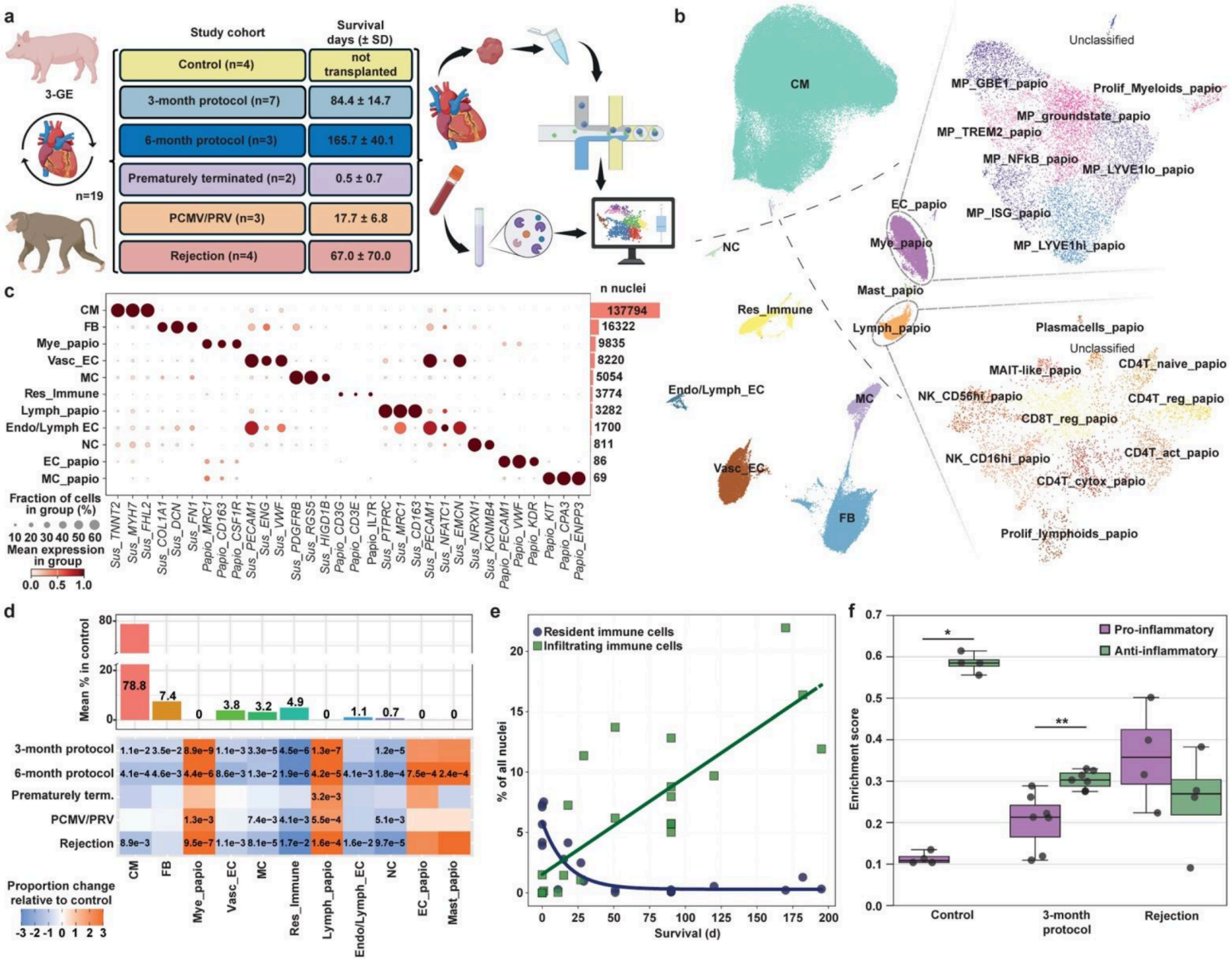

Figure 1

Experimental design and cellular landscape of preclinical cardiac xenografts. (a) Study design and cohort overview of the preclinical pig-to-baboon model (3-GE porcine xenograft). Left and middle panels: schematic representation of experimental cohorts and survival time (mean ± s.d., days). Right panel: workflow for single-nucleus RNA sequencing (snRNA-seq) and plasma proteomic analyses. **(b)** UMAP embedding of 186,947 nuclei reveals eleven cardiac cell types, including seven of *Sus scrofa* and four of *Papio anubis/hamadryas* origin (indicated by "_papio"). Insets display immune subclusters comprising nine myeloid and eleven lymphoid cell states of *Papio* origin (cropping of UMAP indicated by dashed lines). **(c)** Dot plot of canonical marker genes defining major cardiac cell types; color intensity reflects normalized expression levels. **(d)** Centered log-ratio (CLR) differential abundance analysis. Upper: mean cell type proportions (%) in control hearts. Lower: CLR-based linear model effect sizes comparing xHTx cohorts to control hearts (orange, increase; blue, decrease relative to control hearts). Significant proportion changes are displayed (FDR < 0.05). *P* values were derived from two-sided *t*-tests on CLR-transformed values and adjusted using the Benjamini-Hochberg method. **(e)** Temporal dynamics of

immune cell composition. Scatter plot showing the proportion of resident (*Sus scrofa* origin, blue) and infiltrating (*Papio anubis/ hamadryas* origin, green) immune cells over survival time (days). Lines represent best-fit models. **(f)** Boxplot of macrophage (MP) polarization signatures using gene set scoring for pro-inflammatory (green) and anti-inflammatory programs (purple) across the control, '3-month protocol', and 'rejection' cohorts. Dots indicate individual samples. Significance determined by Mann-Whitney U-test with Benjamini-Hochberg correction (* FDR<0.05, ** FDR<0.01). | GE: Genetically engineered, PCMV/PRV: Porcine cytomegalovirus/porcine roseolovirus, CM: Cardiomyocytes, NC: Neuronal cells, Res_Immune: Resident immune cells, Endo/Lymph: Endocardial/Lymphatic, Vasc: Vascular, EC: Endothelial cells, MC: Mural cells, FB: Fibroblasts, Mast: Mast cells, Mye: Myeloids, Lymph: Lymphoids, Papio: *Papio anubis/hamadryas*, Sus: *Sus scrofa*, MP: Macrophage, ISG: Interferon stimulated genes, NK: Natural killer cells, CD4T: CD4 positive T-cells, CD8T: CD8 positive T-cells, MAIT: Mucosal-associated invariant T cells, Reg: regulatory, Act: activated, Cytox: cytotoxic, Prolif: Proliferating, term.: terminated, DEG: Differentially expressed genes, UMAP: Uniform manifold approximation and projection, CLR: Centered log-ratio, SD: Standard deviation, d: days, n: number

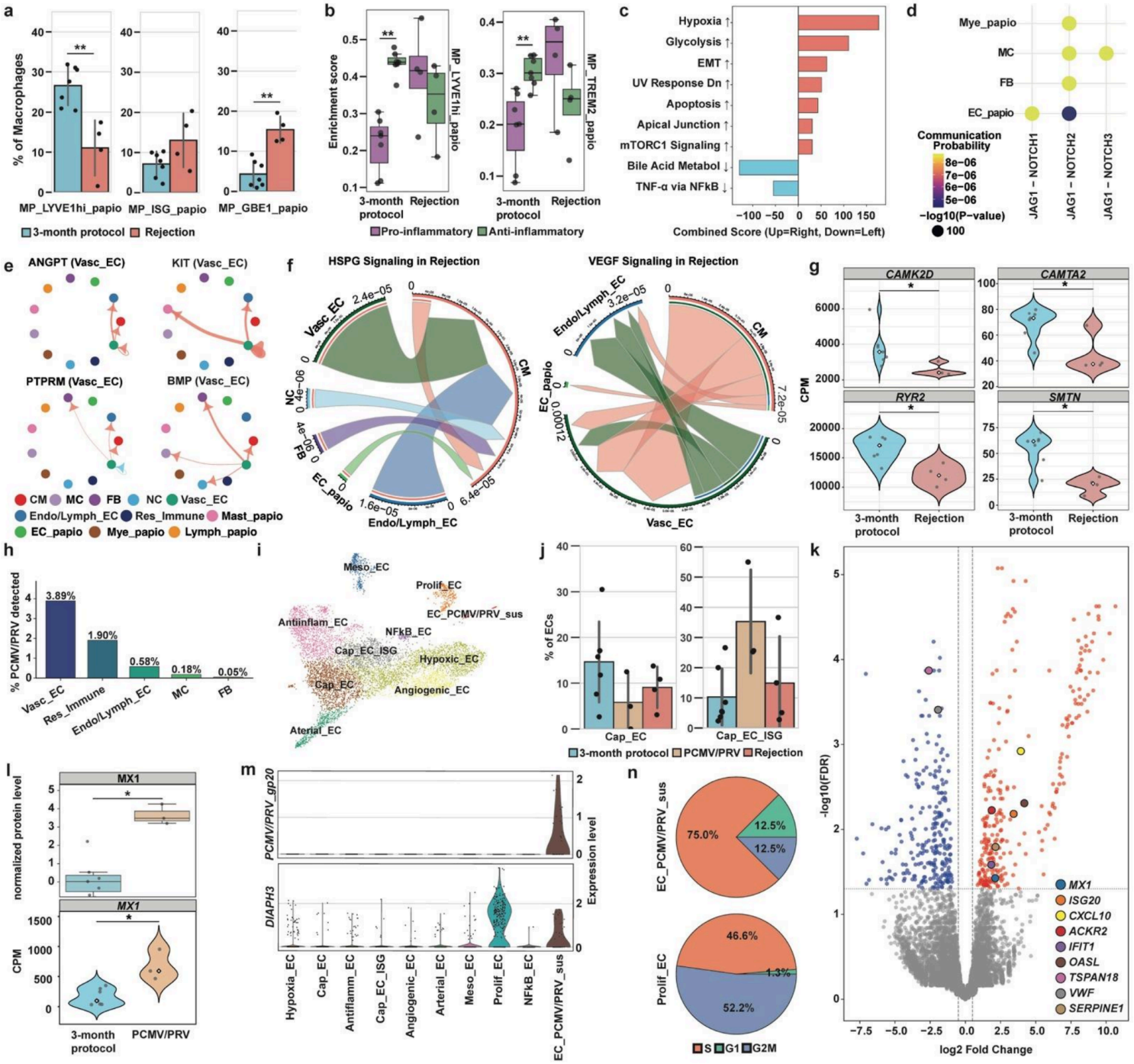

Figure 2

Immune dysregulation and EC response in 'rejection' and 'PCMV/PRV' xenografts. (a) Proportions of MP_LYVE1hi_papio, MP_ISG_papio, and MP_GBE1_papio in '3-month protocol' and rejection xenografts. *P* values were derived from two-sided t-tests on coefficients from CLR ('rejection' vs '3-month protocol'). * and ** reflect *P* value≤0.05, *P* value≤0.01, respectively. **(b)** Gene set scores of proinflammatory (green) and anti-inflammatory (purple) macrophage signatures in Mye_papio in '3-month protocol' and 'rejection' xenografts. Dots represent individual samples. Statistical testing as in (a). **(c)** Pathway enrichment in Mye_papio of rejection xenografts. Bars represent combined enrichment scores (red, upregulated; blue, downregulated). **(d)** Bubble plot of NOTCH pathway ligand-receptor interactions originating from

Vasc_ECs in ‘3-month protocol’ xenografts (absent in rejection). Bubble size displays statistical significance (−log10 (*P* values)), and color intensity indicates communication probability. **(e)** Circle plots showing differential intercellular signaling pathways between ‘rejection’ and ‘3-month protocol’ (salmon, upregulated in rejection; blue, upregulated in ‘3-month protocol’). Arrow directions indicate signaling flow. Line thickness reflects interaction strength. Significance was determined by non-parametric permutation testing (*P* values≤0.05). **(f)** Circos plots showing source-target interaction probabilities of HSPG and VEGF across cell types in rejection. Arrow thickness reflects interaction probability, and colors denote signal sources. **(g)** Violin plots showing pseudobulk expression (counts per million, CPM) of selected genes in ‘rejection’ versus ‘3-month protocol’ xenografts. Statistical testing was done by the Mann-Whitney U test, and a *P* value<0.05 was considered statistically significant. Dots represent individual samples. **(h)** Proportion of nuclei with detectable PCMV/PRV transcripts across cell types. Viral positivity was defined by ≥2 unique PCMV/PRV genes and ≥10 counts. **(i)** UMAP embedding of 8,220 nuclei revealing ten Vasc_ECs cell states. **(j)**Relative proportions of Cap_EC and Cap_EC_ISG states across ‘3-month protocol’, ‘PCMV/PRV’, and ‘rejection’ cohorts. Statistics as in (a). **(k)** Volcano plot of differentially expressed genes (DEGs) in Vasc_ECs (‘PCMV/PRV’ vs. ‘3-month protocol’). Significance was determined by |log2FC|>0.5 and FDR<0.05 (Red: Significantly upregulated, Blue: Significantly downregulated, chosen DEGs additionally colored). **(l)** Expression of MX1 at protein (plasma proteomics; upper) and transcript (Vasc_EC; lower) levels in ‘3-month protocol’ vs. ‘PCMV/PRV’ xenografts. Statistics as in (g). **(m)** Violin plot depicting expression of *PCMV/PRV_gp20* and *DIAPH3* across Vasc_EC states. **(n)** Cell-cycle distribution of proliferative ECs (Prolif_EC) and PCMV/PRV-positive ECs (EC_PCMV/PRV_sus). Pie chart segments represent S-phase (orange), G1 (green), and G2/M (blue); percentages are indicated within each segment. | MP: Macrophages, ISG: Interferon stimulated genes, EMT: Epithelial-to-mesenchymal transition, CM: Cardiomyocytes, NC: Neuronal cells, Res_Immune: Resident immune cells, Endo/Lymph: Endocardial/Lymphatic, Vasc: Vascular, EC: Endothelial cells, MC: Mural cells, FB: Fibroblasts, Mast: Mast cells, Mye: Myeloids, Lymph: Lymphoids, Papio: *Papio anubis/hamadryas,* PCMV/PRV: Porcine cytomegalovirus/porcine roseolovirus, Meso: Mesothelial, Antiinflam: Antiinflammatory, Prolif: Proliferating, Cap: Capillary, S: Synthesis phase, G1: Gap 1, G2M: Gap 2 to mitotic phase, DEG: Differentially expressed genes, UMAP: Uniform manifold approximation and projection, CLR: Centered log-ratio, FC: Fold change, CPM: Counts per million, FDR: False discovery rate.

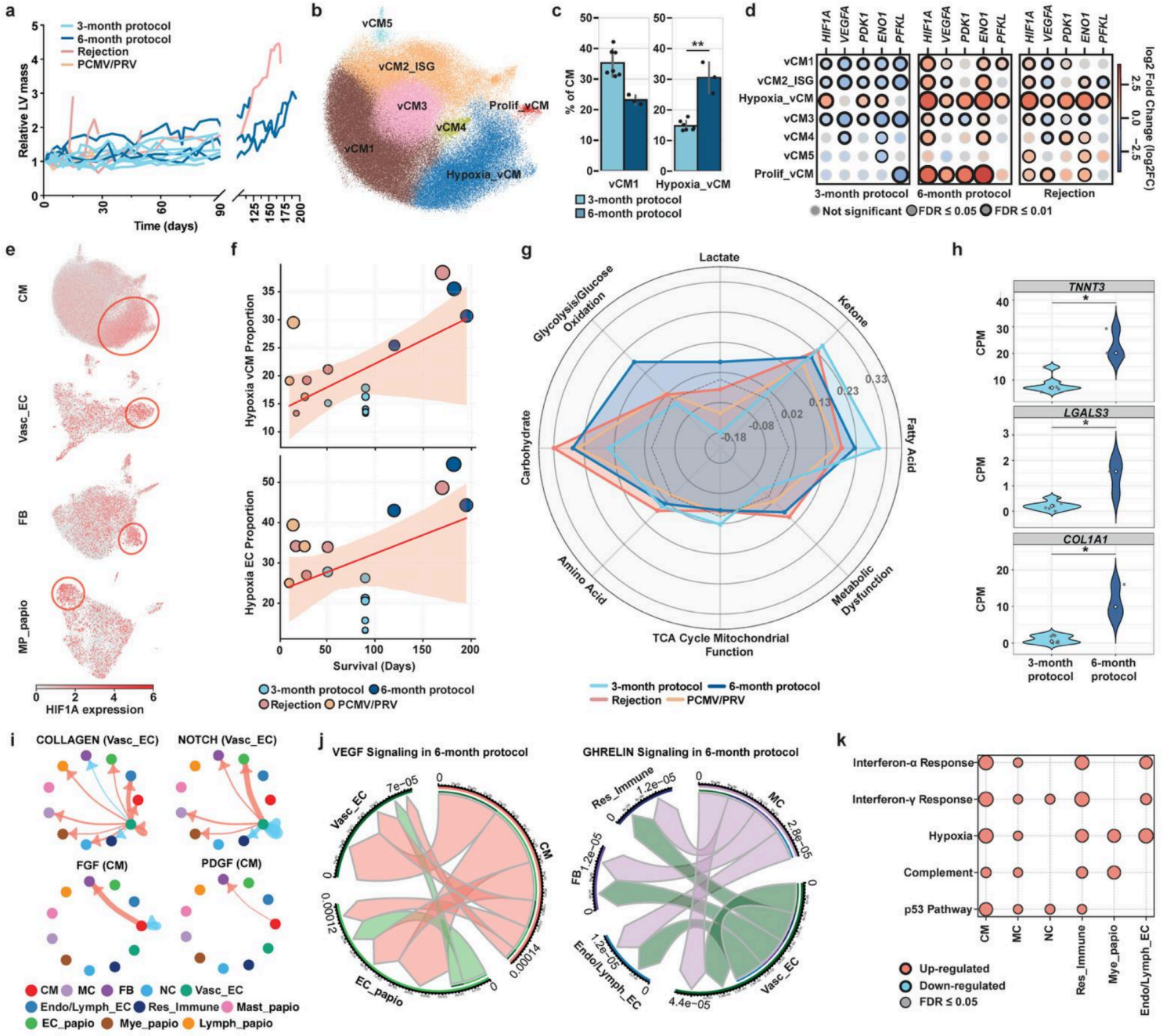

Figure 3

Hypoxia and hypertrophy signaling in '6-month protocol' xenografts. (a) Time course of relative LV mass after xHTx; x-axis break between days 90-100.**(b)** UMAP embedding of CMs showing seven cell states. **(c)** Proportions of vCM1 and Hypoxia_vCM states in '3-month protocol' and '6-month protocol'. *P* values were derived from two-sided t-tests on coefficients from CLR (* *P*value≤0.05). **(d)** Differential expression of hypoxia-associated genes in CM states relative to control hearts. Dot colors reflect log2FC, and dot sizes indicate absolute log2FC. Black circles indicate significance (FDR<0.05 or FDR<0.01). *P* values were calculated using the quasi-likelihood *F*-test with Benjamini-Hochberg correction. **(e)** Feature plots of *HIF1A* expression across all cell types (intensified red reflects higher normalized expression, hotspots circled). **(f)** Temporal increase of hypoxia-vCM and hypoxia_EC cell states over time. **(g)** Spider plot of CM metabolic pathways gene set scores; glycolysis predominates in '6-month protocol' xenografts.

(h) Violin plots of CM genes *TNNT3*, *LGALS3*, and *COL1A1* in '3-month vs '6-month protocol' xenografts. Statistical testing was done by the Mann-Whitney U test, and a *P* value<0.05 was considered statistically significant. Dots represent individual samples. **(i)** Circle plots showing differential intercellular signaling pathways between '6-month protocol' and '3-month protocol' (salmon, upregulated in '6-month protocol'; blue, upregulated in '3-month protocol'). Arrow directions indicate signaling flow. Line thickness reflects interaction strength. Significance was determined by non-parametric permutation testing (*P* values≤0.05). **(j)**Circos plots showing source-target interaction probabilities of VEGF and GHRELIN across cell types in '6-month protocol' xenografts. Arrow thickness shows interaction probability, and colors reflect signal sources. **(k)** Top five upregulated pathways shared across ≥2 cell types in '6-month protocol' xenografts using MSigDB. Bubble size indicates $-\log_{10}$(FDR). | LV: Left ventricular, PCMV/PRV: porcine cytomegalovirus/porcine roseolovirus, vCM: Ventricular cardiomyocytes, CM: Cardiomyocytes, NC: Neuronal cells, Res_Immune: Resident immune cells, Endo/Lymph: Endocardial/Lymphatic, Vasc: Vascular, EC: Endothelial cells, MC: Mural cells, FB: Fibroblasts, Mast: Mast cells, Mye: Myeloids, Lymph: Lymphoids, Papio: *Papio anubis/hamadryas,* TCA: tricarboxylic acid cycle, xHTx: Cardiac xenotransplantation, UMAP: Uniform manifold approximation and projection, CLR: Centered log-ratio, ISG: Interferon stimulated genes, CPM: Counts per million, FDR: False discovery rate.

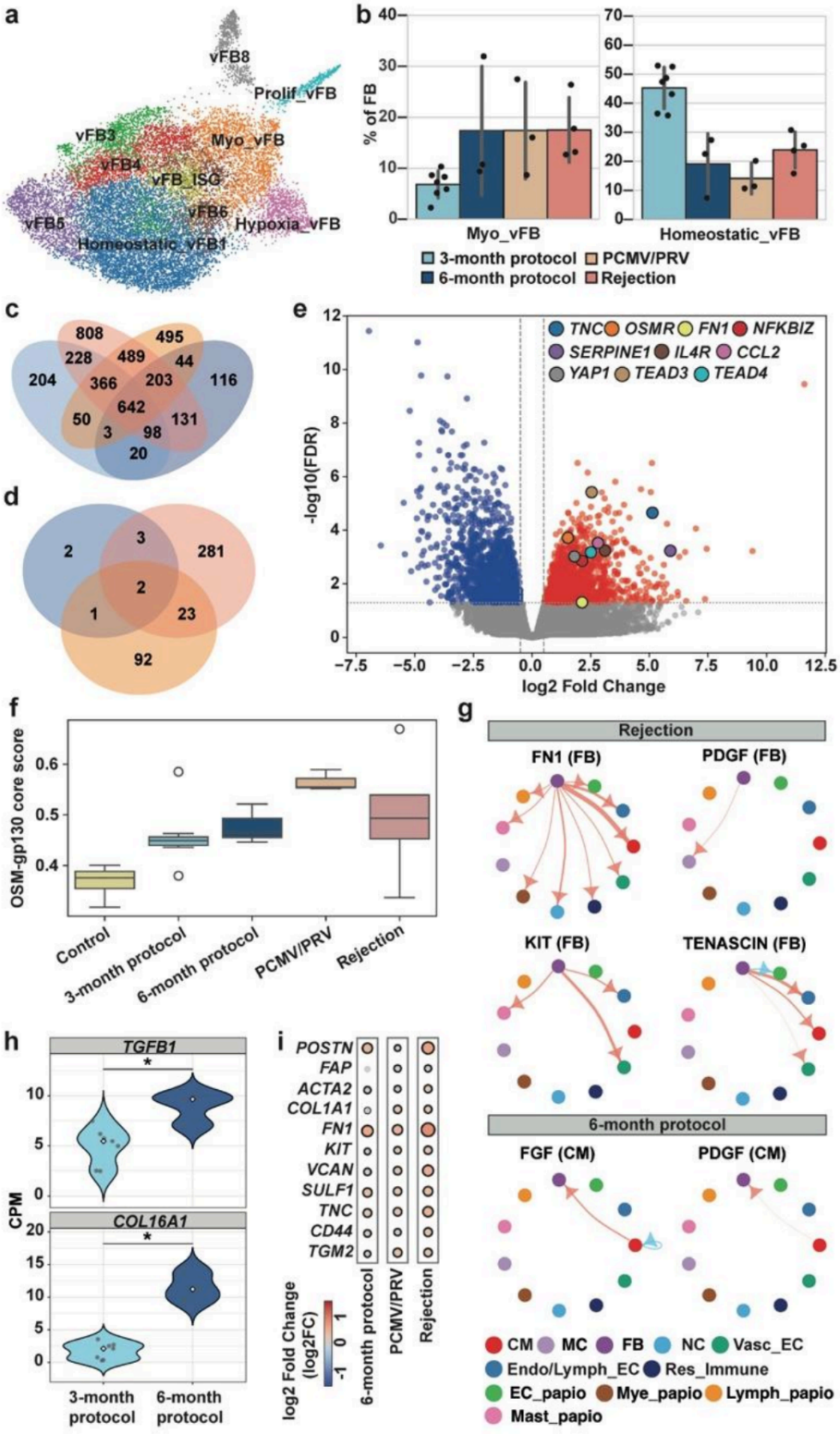

Figure 4

Fibroblast activation and pro-fibrotic initiation across xHTx groups. (a) UMAP of ten FB cell states. **(b)** Abundances of Myo_vFB and Homeostatic_vFB cell states in '3-month protocol', '6-month protocol', 'PCMV/PRV' and 'rejection' cohorts. *P* values calculated by Mann-Whitney U-test and multiple testing correction by Benjamini-Hochberg (* FDR≤0.05). **(c)** Venn diagram showing the abundance of FBs' DEGs in xenografts vs. control hearts. **(d)** Venn diagram showing the abundance of FBs' DEGs in the 'rejection',

‘PCMV/PRV’, and ‘6-month protocol’ cohorts vs. the ‘3-month protocol’ cohort. **(e)** Volcano plot showing DEGs of FBs in xenografts vs control hearts comparison (red: significantly upregulated, blue: significantly downregulated, chosen DEGs additionally colored). Significance was determined by |log2FC|>0.5 and FDR<0.05. **(f)** Gene set scores of OSM-gp130 across the control, ‘3-month protocol’, ‘6-month protocol’, ‘PCMV/PRV’ and ‘rejection’ cohorts. Statistics as in (b). **(g)** Differential cell-cell communication between ‘rejection’ and ‘3-month protocol’ (upper panel) and ‘6-month protocol’ and ‘3-month protocol’ (lower panel) xenografts. Arrows indicate signaling direction. Line thickness reflects interaction strength. Significance was determined by non-parametric permutation testing (*P* values≤0.05). Salmon: increased; blue: decreased. **(h)** Violin plots of CM genes *TGFB1* and *COL16A1* in ‘6-month protocol’ vs ‘3-month protocol’ xenografts. Statistics as in (b). **(i)** Differential expression of pro-fibrotic genes in FBs in ‘6-month protocol’, ‘PCMV/PRV’ and ‘rejection’ cohorts relative to ‘3-month protocol’ samples (dot color: log2FC; dot size: absolute log2FC; *P values*: quasi-likelihood *F*-test with Benjamini-Hochberg correction; black circles indicate FDR≤0.05. | vFB: Ventricular Fibroblasts, Prolif: Proliferating, Myo_FB: Myofibroblasts, ISG: Interferon stimulated genes, FB: Fibroblasts, OSM: Oncostatin M, CM: Cardiomyocytes, NC: Neuronal cells, Res_Immune: Resident immune cells, Endo/Lymph: Endocardial/Lymphatic, Vasc: Vascular, EC: Endothelial cells, MC: Mural cells, Mast: Mast cells, Mye: Myeloids, Lymph: Lymphoids, FC: Fold change, DEG: Differentially expressed genes, CPM: Counts per million, FDR: False discovery rate.

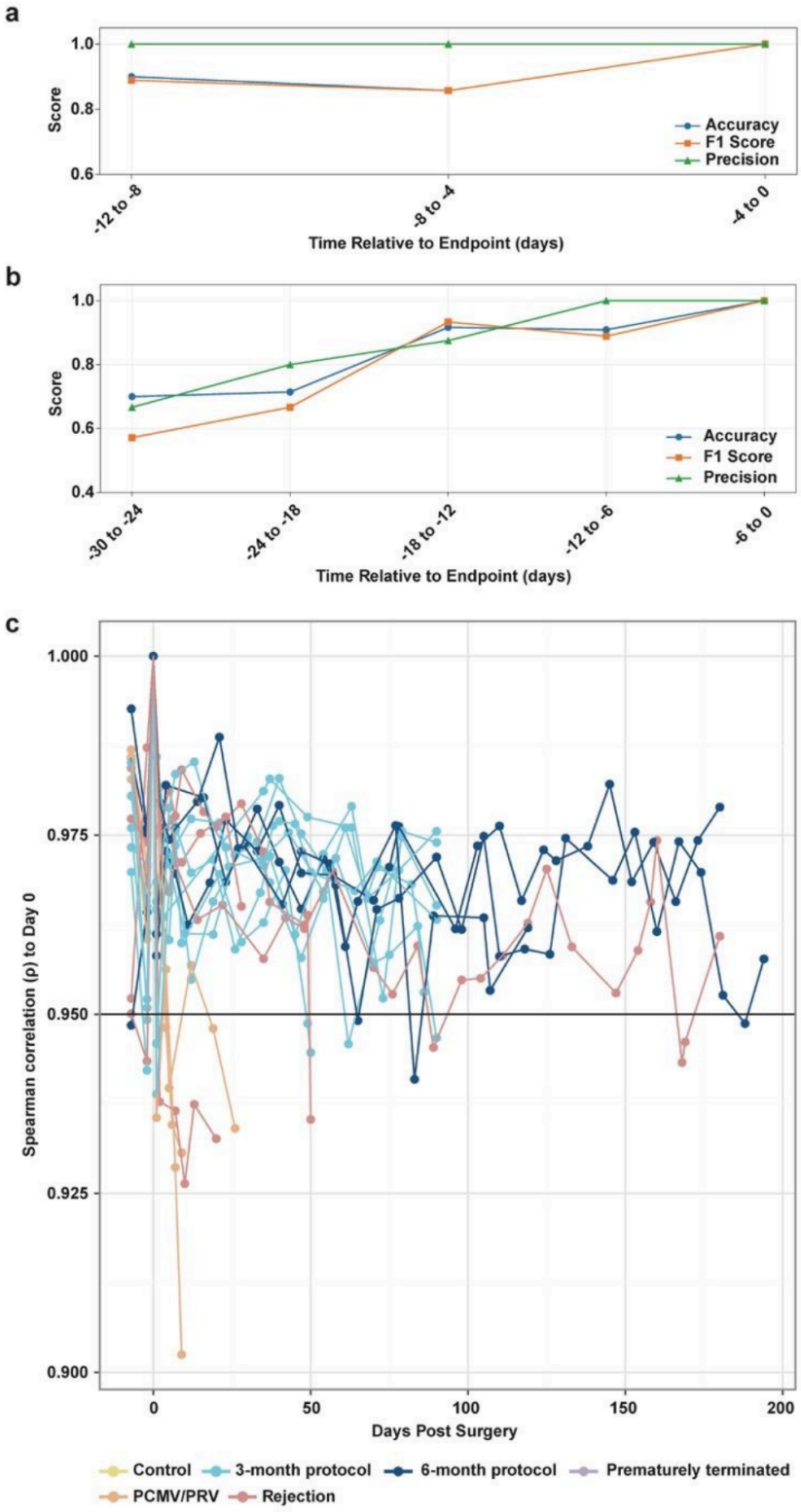

Figure 5

Early prediction of rejection- and PCMV/PRV-associated complications using proteomic signature. Binary classification performance of plasma proteomic samples across time windows relative to the study endpoint. Shown for the '3-month protocol' compared with **(a)** the 'PCMV/PRV' and **(b)** the 'rejection' cohorts. The x-axis indicates non-overlapping time windows prior to the study endpoint used for testing. The classifier was trained on endpoint plasma proteomic signatures and evaluated on earlier

time windows. Accuracy (blue), F1-score (orange) and precision (green) are shown as performance metrics. **(c)** Longitudinal stability of plasma proteomic measurements. Each dot represents a single proteomic measurement; lines represent individual baboons colored by condition. Pairwise spearman rank correlation was calculated relative to the baseline (Day 0; day of surgery) sample from the same baboon. | PCMV/PRV: Porcine cytomegalovirus/porcine roseolovirus.

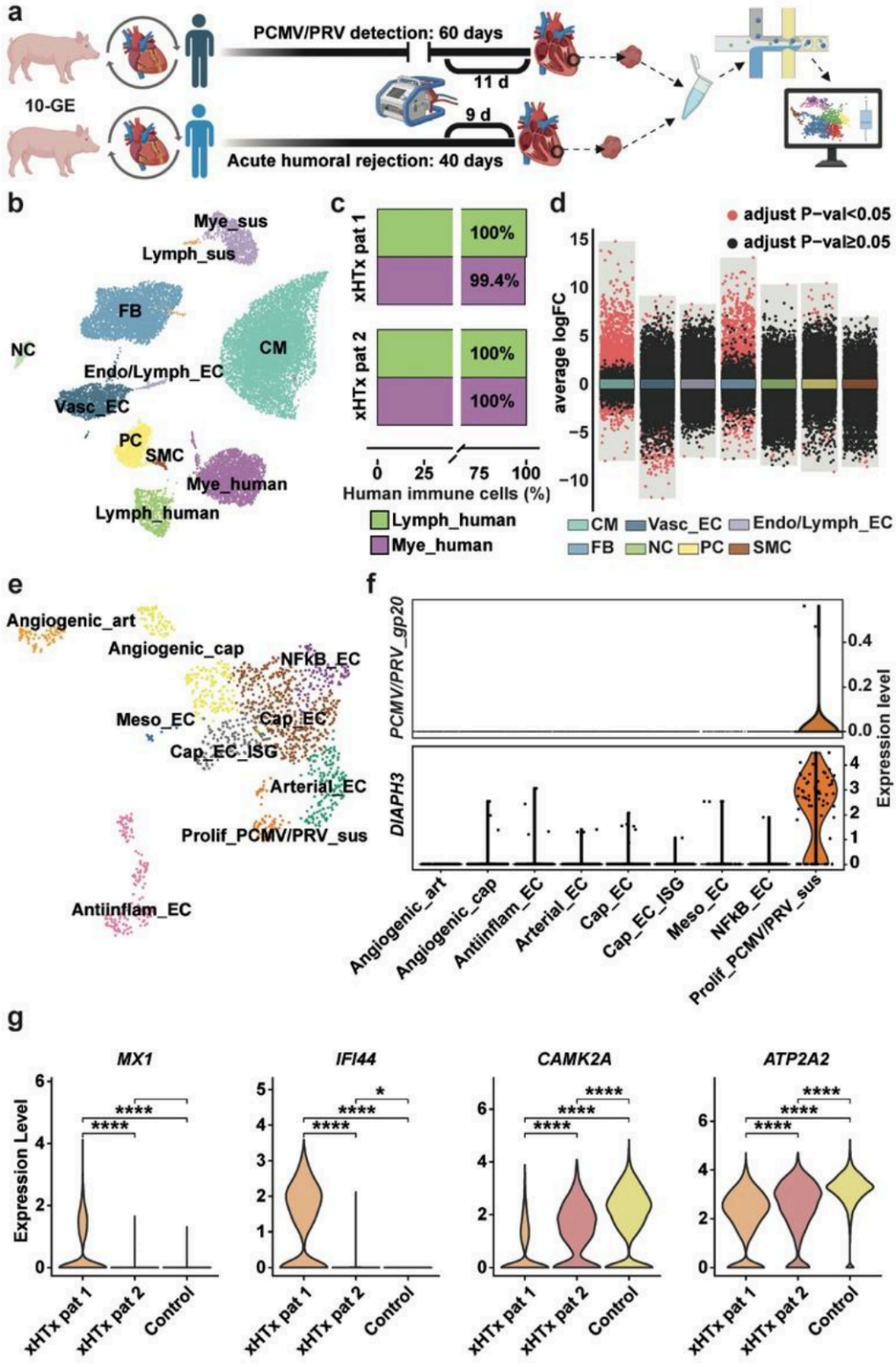

Figure 6

Single-nucleus RNA sequencing landscape of pig-to-human cardiac xenotransplantation. (a) Study design and cohort overview of two pig-to-human xHTx samples (10-GE porcine xenograft). Left and middle panels: schematic of study groups and survival time. Right panel: workflow for snRNA-seq. **(b)** UMAP embedding of 20,289nuclei reveals eleven cardiac cell types, including nine of *Sus scrofa*and two of human origin (indicated by 'human'). **(c)** Proportion of human lymphoids and myeloids in clinical xHTx patients. **(d)** Comparative volcano plot demonstrating DEGs across cell types of clinical xHTx vs control analysis. **(e)** UMAP of ten Vasc_EC cell states. **(f)** Violin plot depicting expression of *PCMV/PRV_gp20* and *DIAPH3* across Vasc_EC states. **(g)** Violin plots showing expression levels of ISGs (*MX1*, *IFI44*) in CMs and calcium handling genes (*CAMK2A*, *ATP2A2*). | GE: Genetically engineered, PCMV/PRV: Porcine cytomegalovirus/porcine roseolovirus, Sus: *Sus scrofa*, Mye: Myeloids, Lymph: Lymphoids, FB: Fibroblasts, CM: Cardiomyocytes, NC: Neuronal cells, Endo/Lymph: Endocardial/Lymphatic, Vasc: Vascular, EC: Endothelial cells, PC: Pericytes, SMC: Smooth muscle cells, art: arterial, cap: capillary, Meso: Mesothelial, ISG: Interferon stimulated genes, Prolif: Proliferating, Antiinflam: Antiinflammatory, pat: patient, P-val: *P*-value, xHTx: Cardiac xenotransplantation, snRNA-seq: Single nucleus RNA sequencing, UMAP: Uniform manifold approximation and projection, DEG: Differentially expressed genes.

Supplementary Files

This is a list of supplementary files associated with this preprint. Click to download.

- SupplementaryTable48.xlsx
- SupplementaryFigure1.pdf
- SupplementaryTable6.xlsx
- SupplementaryTable42.xlsx
- SupplementaryTable20.xlsx
- SupplementaryTable9.xlsx
- SupplementaryFigure5.pdf
- SupplementaryFigure2.pdf
- SupplementaryTable26.csv
- SupplementaryTable15.xlsx
- SupplementaryTable8.xlsx
- SupplementaryTable41.xlsx
- SupplementaryTable43.xlsx
- ExtendedDataTable2.xlsx
- SupplementaryTable4.xlsx
- SupplementaryTable7.xlsx
- SupplementaryTable11.xlsx

- SupplementaryTable19.xlsx
- SupplementaryTable28.xlsx
- SupplementaryTable17.csv
- SupplementaryTable51.txt
- SupplementaryFigure10.pdf
- SupplementaryTable47.xlsx
- SupplementaryTable38.xlsx
- SupplementaryTable13.xlsx
- SupplementaryTable12.csv
- SupplementaryFigure7.pdf
- SupplementaryTable35.xlsx
- SupplementaryTable10.xlsx
- SupplementaryFigure9.pdf
- SupplementaryTable1.xlsx
- SupplementaryTable16.xlsx
- SupplementaryTable18.xlsx
- SupplementaryTable24.xlsx
- SupplementaryTable40.csv
- SupplementaryTable33.xlsx
- SupplementaryFigure8.pdf
- SupplementaryTable44.xlsx
- SupplementaryTable46.xlsx
- SupplementaryTable2.xlsx
- SupplementaryFigure3.pdf
- SupplementaryTable25.xlsx
- SupplementaryTable36.xlsx
- SupplementaryTable32.xlsx
- SupplementaryTable29.xlsx
- SupplementaryTable27.xlsx
- SupplementaryTable5.xlsx
- SupplementaryTable34.xlsx
- SupplementaryTable50.xlsx
- SupplementaryTable22.xlsx
- SupplementaryTable23.xlsx

- SupplementaryFigure6.pdf
- SupplementaryTable31.xlsx
- SupplementaryTable14.xlsx
- SupplementaryFigure4.pdf
- SupplementaryTable30.xlsx
- SupplementaryTable3.xlsx
- SupplementaryTable21.xlsx
- SupplementaryTable45.xlsx
- ExtendedDataTable3.xlsx
- SupplementaryTable49.xlsx
- ExtendedDataTable1.xlsx
- SupplementaryTable39.xlsx
- SupplementaryTable37.xlsx
- ExtendedDataTable4.xlsx
- ExtendedFigures.docx